



Calculation of predictions for non-identical particle correlations in heavy ions collisions at LHC energies from hydrodynamics-inspired models

MASTER OF SCIENCE THESIS

Author:
Mateusz Wojciech Gałażyn

Supervisor:
Prof. Adam Kisiel

Warsaw, 11th November 2014



Wyznaczenie przewidywań teoretycznych dla korelacji cząstek nieidentycznych w zderzeniach ciężkich jonów przy energiach LHC w modelach opartych na hydrodynamice

PRACA MAGISTERSKA

Autor:
Mateusz Wojciech Gałażyn

Promotor:
dr hab. inż. Adam Kisiel, prof. PW

Warszawa, 11 listopada 2014

Abstract

Streszczenie

Contents

1	Theory of heavy ion collisions	2
1.1	The Standard Model	2
1.2	Quantum Chromodynamics	3
1.2.1	Quarks and gluons	3
1.2.2	Quantum Chromodynamics potential	4
1.2.3	The quark-gluon plasma	6
1.3	Relativistic heavy ion collisions	7
1.3.1	Stages of heavy ion collision	7
1.3.2	QGP signatures	9
2	Terminator model	17
2.1	(3+1)-dimensional viscous hydrodynamics	17
2.2	Statistical hadronization	18
2.2.1	Cooper-Frye formalism	19
3	Particle interferometry	21
3.1	HBT interferometry	21
3.2	Theoretical approach	22
3.2.1	Conventions used	22
3.2.2	Two particle wave function	23
3.2.3	Source emission function	24
3.2.4	Theoretical correlation function	26
3.2.5	Spherical harmonics decomposition of a correlation function	27
3.3	Experimental approach	28
3.4	Scaling of femtoscopic radii	29
3.4.1	Scaling in LCMS	30
3.4.2	Scaling in PRF	30
4	Results	32
4.1	Identical particles correlations	32
4.1.1	Spherical harmonics components	32
4.1.2	Centrality dependence of a correlation function	36
4.1.3	k_T dependence of a correlation function	37

34	4.2 Results of the fitting procedure	38
35	4.2.1 The three-dimensional femtoscopic radii scaling	38
36	4.2.2 Scaling of one-dimensional radii	42
37	4.3 Discussion of the results	43
38	5 Summary	44

³⁹ **Introduction**

⁴⁰ **Chapter 1**

⁴¹ **Theory of heavy ion collisions**

⁴² **1.1 The Standard Model**

⁴³ In the 1970s, a new theory of fundamental particles and their interaction
⁴⁴ emerged. A new concept, which concerns the electromagnetic, weak and strong
⁴⁵ nuclear interactions between known particles. This theory is called *The Standard*
⁴⁶ *Model*. There are seventeen named particles in the standard model, organized
⁴⁷ into the chart shown below (Fig. 1.1). Fundamental particles are divided into
two families: *fermions* and *bosons*.

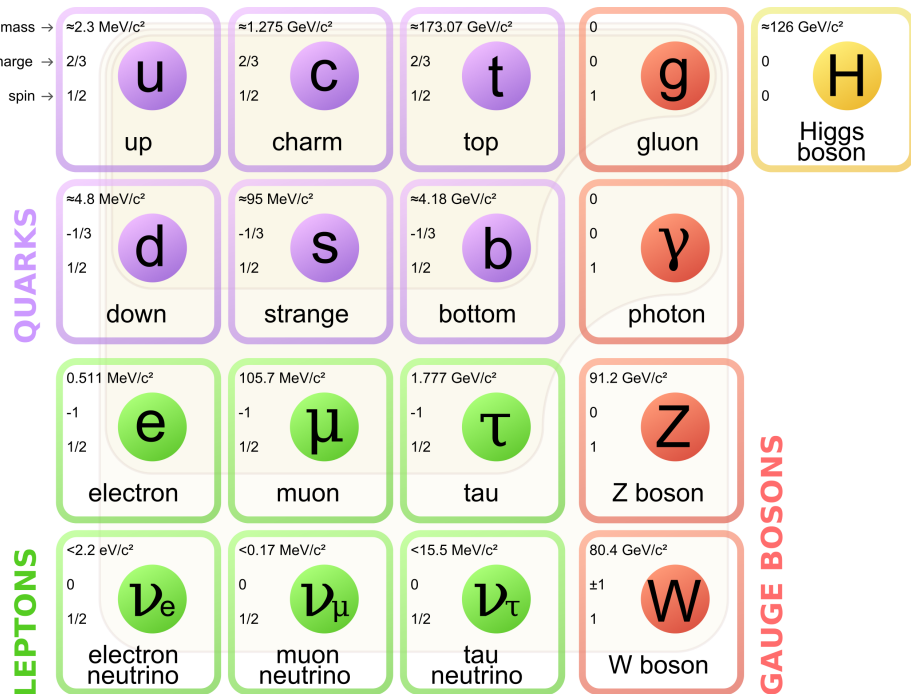


Figure 1.1: The Standard Model of elementary particles [1].

48 Fermions are the building blocks of matter. They are divided into two groups.
 49 Six of them, which must bind together are called *quarks*. Quarks are known to
 50 bind into doublets (*mesons*), triplets (*baryons*) and recently confirmed four-quark
 51 states.¹ Two of baryons, with the longest lifetimes, are forming a nucleus: a pro-
 52 ton and a neutron. A proton is build from two up quarks and one down, and
 53 neutron consists of two down quarks and one up. A proton is found to be a stable
 54 particle (at least it has a lifetime larger than 10^{35} years) and a free neutron has a
 55 mean lifetime about 8.8×10^2 s. Fermions, that can exist independently are called
 56 *leptons*. Neutrinos are a subgroup of leptons, which are only influenced by weak
 57 interaction. Fermions can be divided into three generations (three columns in
 58 the Figure 1.1). Generation I particles can combine into hadrons with the longest
 59 life spans. Generation II and III consists of unstable particles which form also
 60 unstable hadrons.

61 Bosons are force carriers. There are four fundamental forces: weak - respons-
 62 ible for radioactive decay, strong - coupling quarks into hadrons, electromagnetic
 63 - between charged particles and gravity - the weakest, which causes the attraction
 64 between particles with a mass. The Standard Model describes the first three. The
 65 weak force is mediated by W^\pm and Z^0 bosons, electromagnetic force is carried by
 66 photons γ and the carriers of a strong interaction are gluons g . The fifth boson is
 67 a Higgs boson which is responsible for giving other particles mass.

68 1.2 Quantum Chromodynamics

69 1.2.1 Quarks and gluons

70 Quarks interact with each other through the strong interaction. The mediator
 71 of this force is a *gluon* - a massless and chargeless particle. In the quantum chro-
 72 modynamics (QCD) - theory describing strong interaction - there are six types of
 73 "charges" (like electrical charges in the electrodynamics) called *colours*. The col-
 74 ours were introduced because some of the observed particles, like Δ^- , Δ^{++} and
 75 Ω^- appeared to consist of three quarks with the same flavour (ddd , uuu and sss
 76 respectively), which was in conflict with the Pauli principle. One quark can carry
 77 one of the three colours (usually called *red*, *green* and *blue*) and antiquark one of
 78 the three anti-colours respectively. Only colour-neutral (or white) particles could
 79 exist. Mesons are assumed to be a colour-anticolour pair, while baryons are *red-*
 80 *green-blue* triplets. Gluons also are colour-charged and there are 8 types of gluons.
 81 Therefore they can interact with themselves [3].

¹The LHCb experiment at CERN in Geneva confirmed recently existence of $Z(4430)$ - a particle consisting of four quarks [2].

82 **1.2.2 Quantum Chromodynamics potential**

83 As a result of that gluons are massless, one can expect, that the static potential
 84 in the QCD will have the similar form like one in the electrodynamics e.g. $\sim 1/r$
 85 (through an analogy to photons). In reality the QCD potential is assumed to have
 86 the form of [3]

$$V_s = -\frac{4}{3} \frac{\alpha_s}{r} + kr, \quad (1.1)$$

87 where the α_s is a coupling constant of the strong force and the kr part is related
 88 with the *confinement*. In comparison to the electromagnetic force, a value of the
 89 strong coupling constant is $\alpha_s \approx 1$ and the electromagnetic one is $\alpha = 1/137$.

90 The fact that quarks does not exist separately, but they are always bound,
 91 is called a confinement. As two quarks are pulled apart, the linear part kr in
 92 the Eq. 1.1 becomes dominant and the potential becomes proportional to the dis-
 93 tance. This situation resembles stretching of a string. At some point, when the
 94 string is so large it is energetically favourable to create a quark-antiquark pair. At
 95 this moment such pair (or pairs) is formed, the string breaks and the confinement
 96 is preserved (Fig. 1.2).

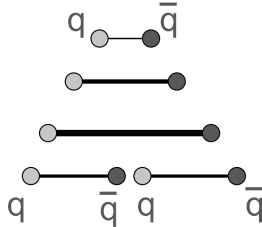


Figure 1.2: A string break and a creation of a pair quark-anti-quark [4].

96 On the other hand, for the small r , an interaction between the quarks and
 97 gluons is dominated by the Coulomb-like term $-\frac{4}{3} \frac{\alpha_s}{r}$. The coupling constant α_s
 98 depends on the four-momentum Q^2 transferred in the interaction. This depend-
 99 ence is presented in Fig. 1.3. The value α_s decreases with increasing momentum
 100 transfer and the interaction becomes weak for large Q^2 , i.e. $\alpha_s(Q) \rightarrow 0$. Be-
 101 cause of weakening of coupling constant, quarks at large energies (or small dis-
 102 tances) are starting to behave like free particles. This phenomenon is known as
 103 an *asymptotic freedom*. The QCD potential has also temperature dependence - the
 104 force strength "melts" with the temperature increase. Therefore the asymptotic
 105 freedom is expected to appear in either the case of high baryon densities (small
 106 distances between quarks) or very high temperatures. This temperature depend-
 107 ence is illustrated in the Fig. 1.4.

108 If the coupling constant α_s is small, one can use perturbative methods to cal-
 109 culate physical observables. Perturbative QCD (pQCD) successfully describes
 110 hard processes (with large Q^2), such as jet production in high energy proton-
 111 antiproton collisions. The applicability of pQCD is defined by the *scale parameter*

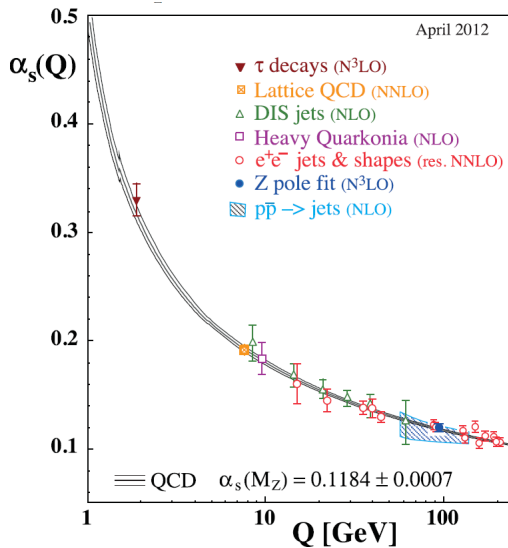


Figure 1.3: The coupling parameter α_s dependence on four-momentum transfer Q^2 [5].

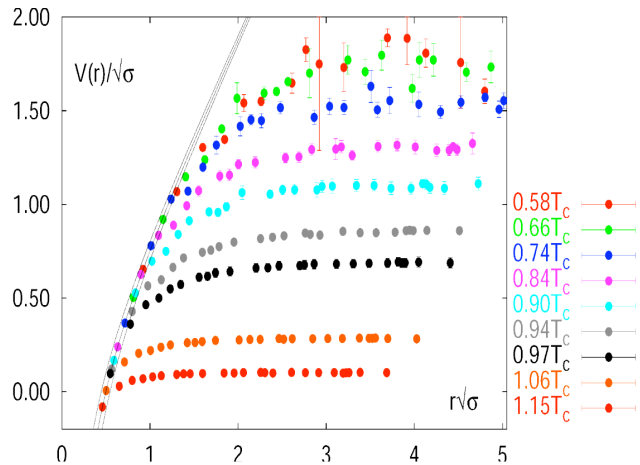


Figure 1.4: The QCD potential for a pair quark-antiquark as a function of distance for different temperatures. A value of a potential decreases with the temperature [4].

¹¹³ $\Lambda_{QCD} \approx 200$ MeV. If $Q \gg \Lambda_{QCD}$ then the process is in the perturbative domain
¹¹⁴ and can be described by pQCD. A description of soft processes (when $Q < 1$ GeV)
¹¹⁵ is a problem in QCD - perturbative theory breaks down at this scale. Therefore,
¹¹⁶ to describe processes with low Q^2 , one has to use alternative methods like Lattice
¹¹⁷ QCD. Lattice QCD (LQCD) is non-perturbative implementation of a field theory
¹¹⁸ in which QCD quantities are calculated on a discrete space-time grid. LQCD al-

lows to obtain properties of matter in equilibrium, but there are some limitations. Lattice QCD requires fine lattice spacing to obtain precise results - therefore large computational resources are necessary. With the constant growth of computing power this problem will become less important. The second problem is that lattice simulations are possible only for baryon density $\mu_B = 0$. At $\mu_B \neq 0$, Lattice QCD breaks down because of the sign problem [6].

1.2.3 The quark-gluon plasma

The new state of matter in which quarks are no longer confined is known as a *quark-gluon plasma* (QGP). The predictions coming from the discrete space-time Lattice QCD calculations reveal a phase transition from the hadronic matter to the quark-gluon plasma at the high temperatures and baryon densities. The res-

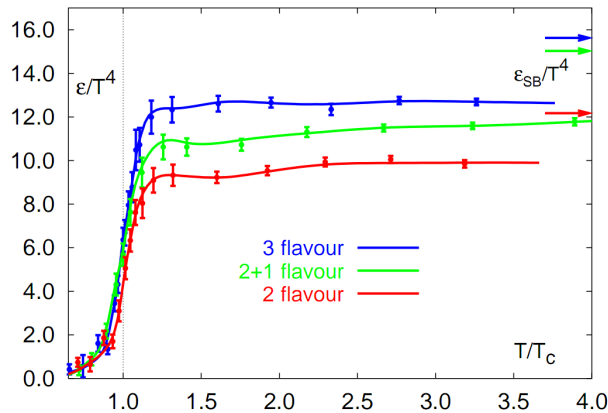


Figure 1.5: A number of degrees of freedom as a function of a temperature [7].

ults obtained from such calculations are shown on Fig. 1.5. The energy density ϵ which is divided by T^4 is a measure of number of degrees of freedom in the system. One can observe significant rise of this value, when the temperature increases past the critical value T_C . Such increase is signaling a phase transition - the formation of QGP [8]. The values of the energy densities plotted in Fig. 1.5 do not reach the Stefan-Boltzmann limit ϵ_{SB} (marked with arrows), which corresponds to an ideal gas. This can indicate some residual interactions in the system. According to the results from the RHIC², the new phase of matter behaves more like an ideal fluid, than like a gas [9].

One of the key questions, to which current heavy ion physics tries to find an answer is the value of a critical temperature T_C as a function of a baryon chemical potential μ_B (baryon density), where the phase transition occur. The results coming from the Lattice QCD are presented in the Fig. 1.6. The phase of matter in which quarks and gluons are deconfined is expected to exist at large

²Relativistic Heavy Ion Collider at Brookhaven National Laboratory in Upton, New York

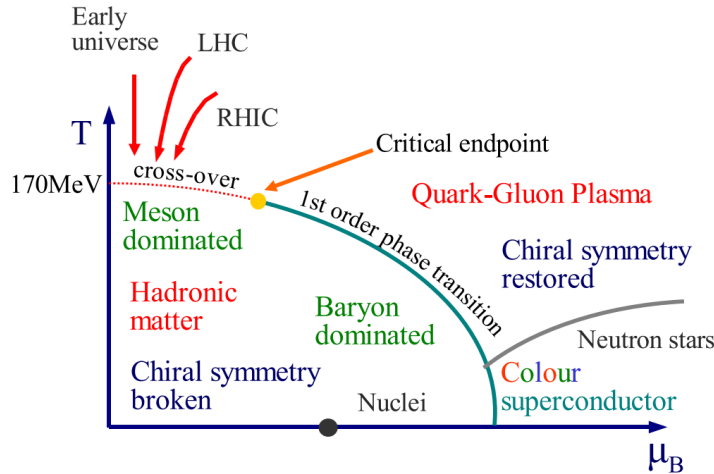


Figure 1.6: Phase diagram coming from the Lattice QCD calculations [8].

temperatures. In the region of small temperatures and high baryon densities, a different state is supposed to appear - a *colour superconductor*. The phase transition between hadronic matter and QGP is thought to be of 1st order at $\mu_B \gg 0$. However as $\mu_B \rightarrow 0$ quarks' masses become significant and a sharp transition transforms into a rapid but smooth cross-over. It is believed that in Pb-Pb collisions observed at the LHC³, the created matter has high enough temperature to be in the quark-gluon plasma phase, then cools down and converts into hadrons, undergoing a smooth transition [8].

1.3 Relativistic heavy ion collisions

1.3.1 Stages of heavy ion collision

To create the quark-gluon plasma one has to achieve high enough temperatures and baryon densities. Such conditions can be recreated in the heavy ion collisions at the high energies. The left side of the Figure 1.7 shows simplified picture of a central collision of two highly relativistic nuclei in the centre-of-mass reference frame. The colliding nuclei are presented as thin disks because of the Lorentz contraction. In the central region, where the energy density is the highest, a new state of matter - the quark-gluon plasma - is supposedly created. Afterwards, the plasma expands ad cools down, quarks combine into hadrons and their mutual interactions cease when the system reaches the *freeze-out* temperature. Subsequently, produced free hadrons move towards the detectors.

On the right side of the Figure 1.7 there is presented a space-time evolution of a collision process, plotted in the light-cone variables (z, t). The two highly

³Large Hadron Collider at CERN, Geneva

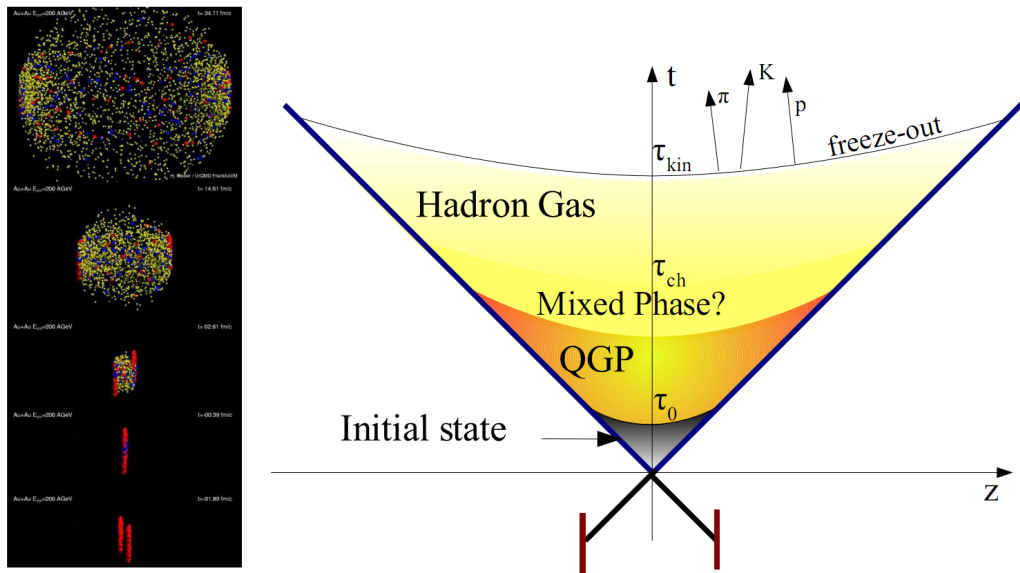


Figure 1.7: Left: stages of a heavy ion collision simulated in the UrQMD model. Right: schematic view of a heavy ion collision evolution [8].

166 relativistic nuclei are traveling basically along the light cone until they collide
 167 at the centre of diagram. Nuclear fragments emerge from the collision again
 168 along the (forward) light cone, while the matter between fragmentation zones
 169 populates the central region. This hot and dense matter is believed to be in the
 170 state of the quark-gluon plasma. There exist several frameworks to describe this
 171 transition to the QGP phase, for example: QCD string breaking, QCD parton cas-
 172 cades or colour glass condensate evolving into glasma and later into quark-gluon
 173 plasma [10].

174 **String breaking** – In the string picture, the nuclei pass through each other forming
 175 colour strings. This is analogous to the situation depicted in the Fig 1.2 - the
 176 colour string is created between quarks inside particular nucleons in nuclei. In
 177 the next step strings decay / fragment forming quarks and gluons or directly
 178 hadrons. This approach becomes invalid at very high energies, when the strings
 179 overlap and cannot be treated as independent objects.

180 **Parton cascade** – The parton⁴ cascade model is based on the pQCD. The col-
 181 liding nuclei are treated as clouds of quarks and which penetrate through each
 182 other. The key element of this method is the time evolution of the parton phase-
 183 space distributions, which is governed by a relativistic Boltzmann equation with
 184 a collision term that contains dominant perturbative QCD interations. The bot-
 185 tleneck of the parton cascade model is the low energies regime, where the Q^2 is
 186 too small to be described by the perturbative theory.

⁴A parton is a common name for a quark and a gluon.

187 **Colour glass condensate** – The colour glass condensate assumes, that the had-
 188 ion can be viewed as a tightly packed system of interacting gluons. The sat-
 189 uration of gluons increases with energy, hence the total number of gluons may
 190 increase without the bound. Such a saturated and weakly coupled gluon system
 191 is called a colour glass condensate. The fast gluons in the condensate are Lorentz
 192 contracted and redistributed on the two very thin sheets representing two col-
 193 liding nuclei. The sheets are perpendicular to the beam axis. The fast gluons
 194 produce mutually orthogonal colour magnetic and electric fields, that only ex-
 195 ist on the sheets. Immediately after the collision, i.e. just after the passage of
 196 the two gluonic sheets after each other, the longitudinal electric and magnetic
 197 fields are produced forming the *glasma*. The glasma fields decay through the
 198 classical rearrangement of the fields into radiation of gluons. Also decays due to
 199 the quantum pair creations are possible. In this way, the quark-gluon plasma is
 200 produced.

201 Interactions within the created quark-gluon plasma bring the system into the
 202 local statistical equilibrium, hence its further evolution can be described by the
 203 relativistic hydrodynamics. The hydrodynamic expansion causes that the sys-
 204 tem becomes more and more dilute. The phase transition from the quark-gluon
 205 plasma to the hadronic gas occurs. Further expansion causes a transition from the
 206 strongly interaction hadronic gas to weakly interacting system of hadrons which
 207 move freely to the detectors. Such decoupling of hadrons is called the *freeze-out*.
 208 The freeze-out can be divided into two phases: the chemical freeze-out and the
 209 thermal one. The *chemical freeze-out* occurs when the inelastic collisions between
 210 constituents of the hadron gas stop. As the system evolves from the chemical
 211 freeze-out to the thermal freeze-out the dominant processes are elastic collisions
 212 (such as, for example $\pi + \pi \rightarrow \rho \rightarrow \pi + \pi$) and strong decays of heavier reso-
 213 nances which populate the yield of stable hadrons. The *thermal freeze-out* is the
 214 stage of the evolution of matter, when the strongly coupled system transforms
 215 to a weakly coupled one (consisting of essentially free particles). In other words
 216 this is the moment, where the hadrons practically stop to interact. Obviously, the
 217 temperatures corresponding to the two freeze-outs satisfy the condition

$$T_{chem} > T_{therm}, \quad (1.2)$$

218 where T_{chem} (inferred from the ratios of hadron multiplicities) is the temperature
 219 of the chemical freeze-out, and T_{therm} (obtained from the investigation of the
 220 transverse-momentum spectra) is the temperature of the thermal freeze-out [10].

221 1.3.2 QGP signatures

222 The quark-gluon plasma is a very short living and unstable state of matter.
 223 One cannot investigate the properties of a plasma and confirm its existence dir-
 224 ectly. Hence, the several experimental effects were proposed as QGP signatures,
 225 some of them have been already observed in heavy ion experiments [8]. As mat-
 226 ter created in the heavy ions collisions is supposed to behave like a fluid, one

should expect appearance of collective behaviour at small transverse momenta - so called *elliptic flow* and *radial flow*. The next signal is the temperature range obtained from the measurements of *direct photons*, which gives us information, that the system created in heavy ion collisions is far above the critical temperature obtained from the LQCD calculations. The *puzzle in the di-lepton spectrum* can be explained by the modification of spectral shape of vector mesons (mostly ρ meson) in the presence of a dense medium. This presence of a medium can also shed light on the *jet quenching* phenomenon - the suppression occurrence in the high p_T domain.

Elliptic flow

In a non-central heavy ion collisions, created region of matter has an almond shape with its shorter axis in the *reaction plane* (Fig. 1.8). The pressure gradient is much larger in-plane rather than out-of-plane. This causes larger acceleration and transverse velocities in-plane rather than out-of-plane. Such differences can

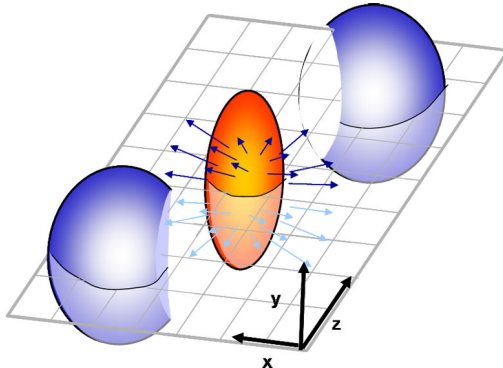


Figure 1.8: Overlapping region which is created in heavy ion collisions has an almond shape. Visible x-z plane is a *reaction plane*. The x-y plane is a *transverse plane*. The z is a direction of the beam [11].

be investigated by studying the distribution of particles with respect to the reaction plane orientation [12]:

$$E \frac{d^3 N}{dp^3} = \frac{1}{2\pi} \frac{d^2 N}{p_T dp_T dy} (1 + 2v_1 \cos(\phi) + 2v_2 \cos(2\phi) + \dots), \quad (1.3)$$

where ϕ is the angle between particle transverse momentum p_T (a momentum projection on a transverse plane) and the reaction plane, N is a number of particles and E is an energy of a particle. The y variable is a *rapidity* defined as:

$$y = \frac{1}{2} \ln \left(\frac{E + p_L}{E - p_L} \right), \quad (1.4)$$

246 where p_L is a longitudinal component of a momentum (parallel to the beam direction).
 247 The v_n coefficients indicate the shape of a system. For the most central collisions
 248 ($b = 0$ - see Fig. 1.9) all coefficients vanish $\bigwedge_{n \in N_+} v_n = 0$ (the overlapping region has the spherical shape). The Fourier series elements in the parentheses

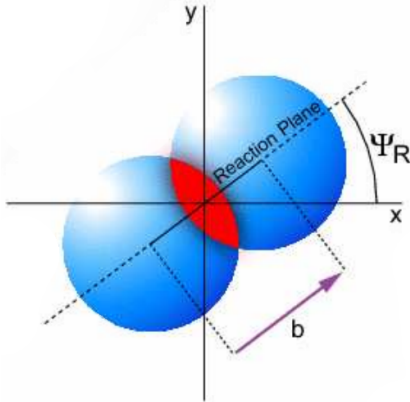


Figure 1.9: Cross-section of a heavy ion collision in a transverse plane. Ψ_R is an angle between transverse plane and the reaction plane. The b parameter is an *impact parameter* - a distance between centers of nuclei during a collision. An impact parameter is related with the centrality of a collision and a volume of the quark-gluon plasma [12].

249 in Eq. 1.3 represent different kinds of a flow. The first value: "1" represents the
 250 *radial flow* - an isotropic flow in every direction. Next coefficient v_1 is responsible
 251 for *direct flow*. The v_2 coefficient is a measure of elliptic anisotropy (*elliptic flow*).
 252 The v_2 has to build up in the early stage of a collision - later the system becomes
 253 too dilute: space asymmetry and the pressure gradient vanish. Therefore the
 254 observation of elliptic flow means that the created matter was in fact a strongly
 255 interacting matter.

256 The v_2 coefficient was measured already at CERN SPS, LHC and RHIC. For
 257 the first time hydrodynamics successfully described the collision dynamics as the
 258 measured v_2 reached hydrodynamic limit (Fig. 1.10). As expected, there is a mass
 259 ordering of v_2 as a function of p_T (lower plot in the Fig. 1.10) with pions having
 260 the largest and protons the smallest anisotropy. In the upper plots in the Fig. 1.10
 261 there is a v_2 as a function of transverse kinetic energy. The left plot shows the
 262 two universal trend lines for baryons and mesons. After the scaling of v_2 and the
 263 kinetic energy by the number of valence quarks, all of the hadrons follow the
 264 same universal curve. Those plots show that strong collectivity is observed in
 265 heavy ion collisions.

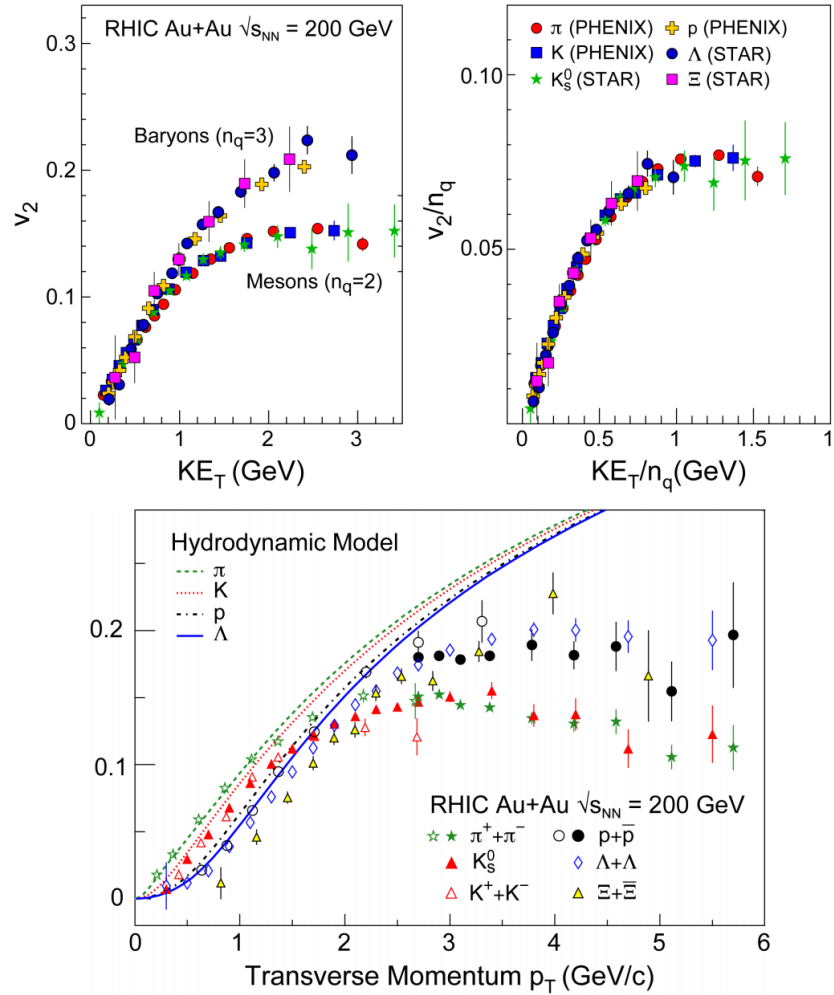


Figure 1.10: *Lower:* The elliptic flow v_2 follows the hydrodynamical predictions for an ideal fluid perfectly. Note that > 99% of all final hadrons have $p_T < 1.5$ GeV/c. *Upper left:* The v_2 plotted versus transverse kinetic energy $KE_T = m_T - m_0 = \sqrt{p_T^2 + m_0^2} - m_0$. The v_2 follows different universal curves for mesons and baryons. *Upper right:* When scaled by the number of valence quarks, the v_2 follows the same universal curve for all hadrons and for all values of scaled transverse kinetic energy [13].

267 Transverse radial flow

268 Elliptic flow described previously is caused by the pressure gradients which
 269 must also produce a more simple collective behaviour of matter - a movement
 270 inside-out, called radial flow. Particles are pushed to higher momenta and they
 271 move away from the center of the collision. A source not showing collective

272 behaviour, like pp collisions, produces particle spectra that can be fitted by a
 273 power-law [8]:

$$\frac{1}{2\pi p_T} \frac{d^2N}{dp_T d\eta} = C \left(1 + \frac{p_T}{p_0} \right)^{-\gamma}. \quad (1.5)$$

274 The η variable is a *pseudorapidity* defined as follows:

$$\eta = \frac{1}{2} \ln \left(\frac{p + p_L}{p - p_L} \right) = -\ln \left(\frac{\theta}{2} \right), \quad (1.6)$$

where θ is an emission angle $\cos \theta = p_L/p$.

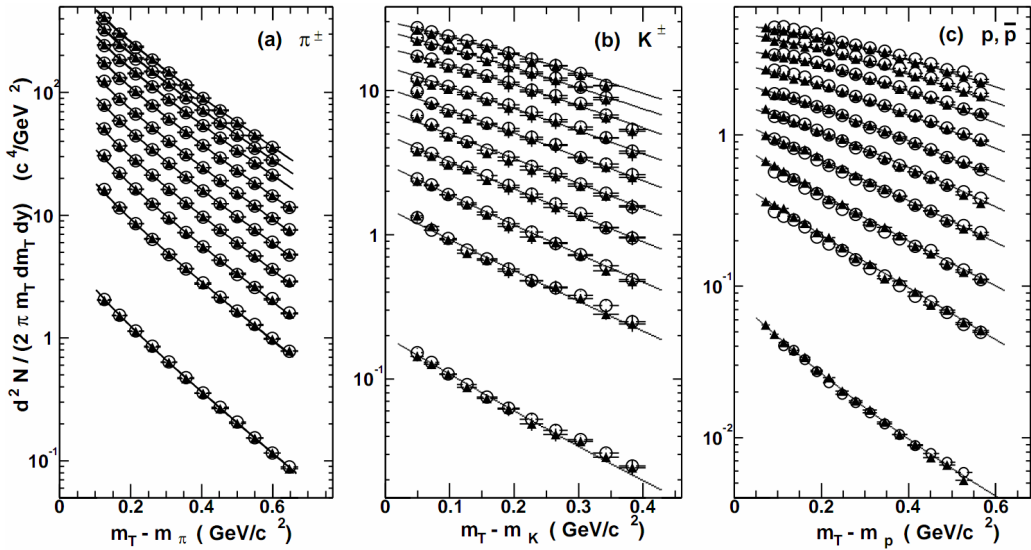


Figure 1.11: Invariant yield of particles versus transverse mass $m_T = \sqrt{p_T^2 + m_0^2}$ for π^\pm , K^\pm , p and \bar{p} at mid-rapidity for p+p collisions (bottom) and Au+Au events from 70-80% (second bottom) to 0-5% (top) centrality [14].

275
 276 The hydrodynamical expansion of a system gives the same flow velocity kick
 277 for different kind of particles - ones with bigger masses will gain larger p_T boost.
 278 This causes increase of the yield of particles with larger transverse momenta. In
 279 the invariant yield plots one can observe the decrease of the slope parameter,
 280 especially for the heavier hadrons. This is presented in the Fig. 1.11. The most
 281 affected spectra are ones of kaons (b) and protons (c). One can notice decrease
 282 of the slope parameter for heavy ion collisions (plots from second bottom to top)
 283 comparing to the proton-proton collisions (bottom ones), where no boost from
 284 radial flow should occur [8].

285 Direct photons

286 The direct photons are photons, which are not coming from the final state
 287 hadrons decays. Their sources can be various interaction from charged particles

288 created in the collision, either at the partonic or at the hadronic level. Direct
 289 photons are considered to be an excellent probe of the early stage of the collision.
 290 This is because their mean free path is very large to the created system in the
 291 collision. Thus photons created at the early stage leave the system without suf-
 292 fering any interaction and retain information about this stage, in particular about
 293 its temperature.

294 One can distinguish two kinds of direct photons: *thermal* and *prompt*. Thermal
 295 photons can be emitted from the strong processes in the quark-gluon plasma in-
 296 volving quarks and gluons or hot hadronic matter (e.g. processes: $\pi\pi \rightarrow \rho\gamma$,
 297 $\pi\rho \rightarrow \pi\gamma$). Thermal photons can be observed in the low p_T region. Prompt
 298 photons are believed to come from “hard” collisions of initial state partons be-
 299 longing to the colliding nuclei. The prompt photons can be described using the
 300 pQCD. They will dominate the high p_T region. The analysis of transverse mo-
 301 mentum of spectra of direct photons revealed, that the temperature of the source
 302 of thermal photons produced in heavy ion collisions at RHIC is in the range 300-
 303 600 MeV (Fig. 1.12). Hence the direct photons had to come from a system whose
 temperature is far above from the critical temperature for QGP creation.

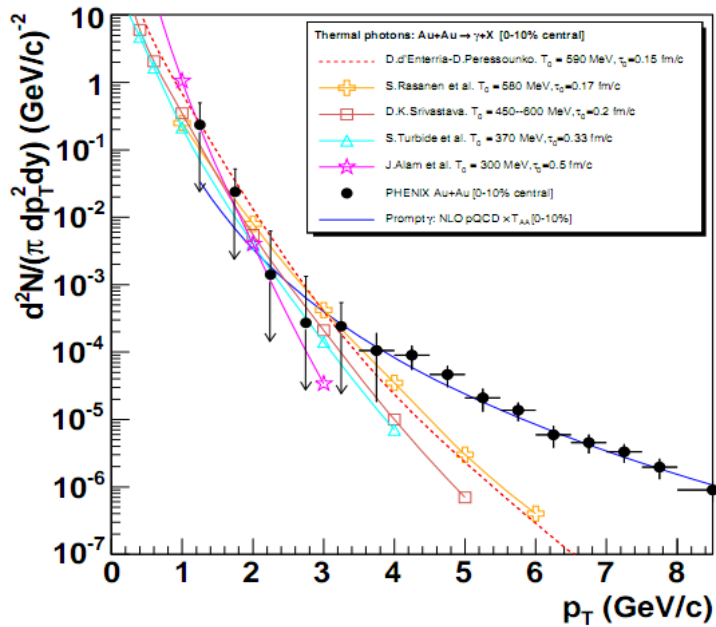


Figure 1.12: Thermal photons spectra for the central Au+Au collisions at $\sqrt{s_{NN}} = 200$ GeV computed within different hydrodynamical models compared with the pQCD calculations (solid line) and experimental data from PHENIX (black dots) [15].

305 **Puzzle in di-lepton mass spectrum**

306 The invariant mass spectra (Fig. 1.13) of lepton pairs reveal many peaks cor-
 307 responding to direct decays of various mesons into a lepton pair. The continu-
 308 ous background in this plot is caused by the decays of hadrons into more than
 309 two leptons (including so-called *Dalitz decays* into a lepton pair and a photon).
 Particular hadron decay channels, which contribute to this spectrum are shown

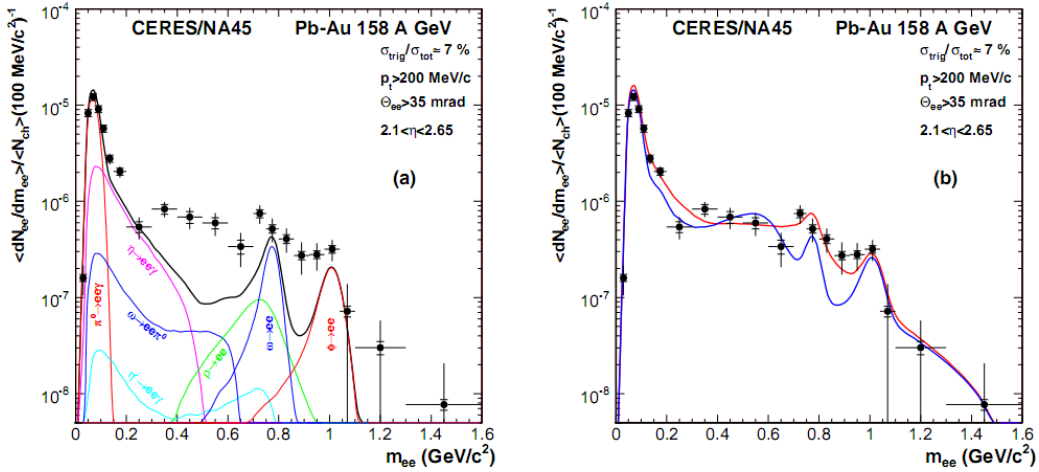


Figure 1.13: Left: Invariant mass spectrum of $e^+ - e^-$ pairs in $\text{Pb} + \text{Au}$ collisions at 158A GeV compared to the sum coming from the hadron decays predictions. Right: The expectations coming from model calculations assuming a dropping of the ρ mass (blue) or a spread of the ρ width in the medium (red) [16].

310 in the Fig. 1.13 with the coloured lines and their sum with the black one. The
 311 sum (called *the hadronic cocktail*) of various components describes experimen-
 312 tal spectra coming from the simple collisions (like $p + p$ or $p + A$) quite well with the
 313 statistical and systematical uncertainties [9]. This situation is different consider-
 314 ing more complicated systems i.e. $A + A$. Spectra coming from $\text{Pb} + \text{Au}$ collisions
 315 are presented on the plots in the Fig. 1.13. The “hadronic cocktail” does not de-
 316 scribe the data, in the mass range between the π and the ρ mesons a significant
 317 excess of electron pairs over the calculated sum is observed. Theoretical expla-
 318 nation of this phenomenon assumes modification of the spectral shape of vector
 319 mesons in a dense medium. Two different interpretations of this increase were
 320 proposed: a decrease of meson mass with the medium density and increase of the
 321 meson width in the dense medium. In principle, one could think of simultaneous
 322 occurrence of both effects: mass shift and resonance broadening. Experimental
 323 results coming from the CERES disfavour the mass shift hypothesis indicating
 324 only broadening of resonance peaks (Fig. 1.13b) [9].

326 **Jet quenching**

327 A jet is defined as a group of particles with close vector momenta and high en-
 328 ergies. It has its beginning when the two partons are going in opposite directions
 329 and have energy big enough to produce new quark-antiquark pair and then ra-
 330 diate gluons. This process can be repeated many times and it results in two back-
 331 to-back jets of hadrons. It has been found that jets in the opposite hemisphere
 332 (*away-side jets*) show a very different pattern in d+Au and Au+Au collisions. This
 333 is shown in the azimuthal correlations in the Fig. 1.14. In d+Au collisions, like in
 334 p+p, a pronounced away-side jet appears around $\Delta\phi = \pi$, exactly opposite to the
 335 trigger jet, what is typical for di-jet events. In central Au+Au collisions the away-
 jet is suppressed. When the jet has its beginning near the surface of the quark-

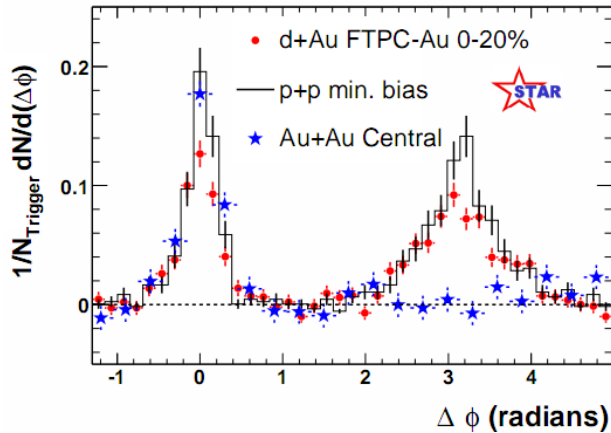


Figure 1.14: Azimuthal angle difference $\Delta\phi$ distributions for different colliding systems at $\sqrt{s_{NN}} = 200$ GeV. Transverse momentum cut: $p_T > 2$ GeV. For the Au+Au collisions the away-side jet is missing [17].

336
 337 gluon plasma, one of the jets (*near-side jet*) leaves the system almost without any
 338 interactions. This jet is visible on the correlation plot as a high peak at $\Delta\phi = 0$.
 339 However, the jet moving towards the opposite direction has to penetrate a dense
 340 medium. The interaction with the plasma causes energy dissipation of particles
 341 and is visible on an azimuthal correlation plot as disappearance of the away-side
 342 jet [9].

³⁴³ **Chapter 2**

³⁴⁴ **Therminator model**

³⁴⁵ THERMINATOR [18] is a Monte Carlo event generator designed to investigate
³⁴⁶ the particle production in the relativistic heavy ion collisions. The functionality
³⁴⁷ of the code includes a generation of the stable particles and unstable resonances
³⁴⁸ at the chosen hypersurface model. It performs the statistical hadronization which
³⁴⁹ is followed by space-time evolution of particles and the decay of resonances. The
³⁵⁰ key element of this method is an inclusion of a complete list of hadronic reso-
³⁵¹ nances, which contribute very significantly to the observables. The second version
³⁵² of THERMINATOR [19] comes with a possibility to incorporate any shape of freeze-
³⁵³ out hypersurface and the expansion velocity field, especially those generated ex-
³⁵⁴ ternally with various hydrodynamic codes.

³⁵⁵ **2.1 (3+1)-dimensional viscous hydrodynamics**

³⁵⁶ Most of the relativistic viscous hydrodynamic calculations are done in
³⁵⁷ (2+1)-dimensions. Such simplification assumes boost-invariance of a matter
³⁵⁸ created in a collision. Experimental data reveals that no boost-invariant region is
³⁵⁹ formed in the collisions [20]. Hence, for the better description of created system
³⁶⁰ a (3+1)-dimensional model is required.

³⁶¹ In the four dimensional relativistic dynamics one can describe a system
³⁶² using a space-time four-vector $x^\nu = (ct, x, y, z)$, a velocity four-vector
³⁶³ $u^\nu = \gamma(c, v_x, v_y, v_z)$ and a energy-momentum tensor $T^{\mu\nu}$. The particular
³⁶⁴ components of $T^{\mu\nu}$ have a following meaning:

- ³⁶⁵ • T^{00} - an energy density,
- ³⁶⁶ • $cT^{0\alpha}$ - an energy flux across a surface x^α ,
- ³⁶⁷ • $T^{\alpha 0}$ - an α -momentum flux across a surface x^α multiplied by c ,
- ³⁶⁸ • $T^{\alpha\beta}$ - components of momentum flux density tensor,

369 where $\gamma = (1 - v^2/c^2)^{-1/2}$ is Lorentz factor and $\alpha, \beta \in \{1, 2, 3\}$. Using u^ν one can
 370 express $T^{\mu\nu}$ as follows [21]:

$$T_0^{\mu\nu} = (e + p)u^\mu u^\nu - pg^{\mu\nu} \quad (2.1)$$

371 where e is an energy density, p is a pressure and $g^{\mu\nu}$ is an inverse metric tensor:

$$g^{\mu\nu} = \begin{bmatrix} 1 & 0 & 0 & 0 \\ 0 & -1 & 0 & 0 \\ 0 & 0 & -1 & 0 \\ 0 & 0 & 0 & -1 \end{bmatrix}. \quad (2.2)$$

372 The presented version of energy-momentum tensor (Eq. 2.1) can be used to de-
 373 scribe dynamics of a perfect fluid. To take into account influence of viscosity,
 374 one has to apply the following corrections coming from shear $\pi^{\mu\nu}$ and bulk Π
 375 viscosities [22]:

$$T^{\mu\nu} = T_0^{\mu\nu} + \pi^{\mu\nu} + \Pi(g^{\mu\nu} - u^\mu u^\nu). \quad (2.3)$$

376 The stress tensor $\pi^{\mu\nu}$ and the bulk viscosity Π are solutions of dynamical equa-
 377 tions in the second order viscous hydrodynamic framework [21]. The compari-
 378 son of hydrodynamics calculations with the experimental results reveal, that the
 379 shear viscosity divided by entropy η/s has to be small and close to the AdS/CFT
 380 estimate $\eta/s = 0.08$ [22, 23]. The bulk viscosity over entropy value used in calcu-
 381 lations is $\zeta/s = 0.04$ [22].

382 When using $T^{\mu\nu}$ to describe system evolving close to local thermodynamic
 383 equilibrium, relativistic hydrodynamic equations in a form of:

$$\partial_\mu T^{\mu\nu} = 0 \quad (2.4)$$

384 can be used to describe the dynamics of the local energy density, pressure and
 385 flow velocity.

386 Hydrodynamic calculations are starting from the Glauber¹ model initial con-
 387 ditions. The collective expansion of a fluid ends at the freeze-out hypersurface.
 388 That surface is usually defined as a constant temperature surface, or equivalently
 389 as a cut-off in local energy density. The freeze-out is assumed to occur at the
 390 temperature $T = 140$ MeV.

391 2.2 Statistical hadronization

392 Statistical description of heavy ion collision has been successfully used
 393 to describe quantitatively *soft* physics, i.e. the regime with the transverse
 394 momentum not exceeding 2 GeV. The basic assumption of the statistical
 395 approach of evolution of the quark-gluon plasma is that at some point of the

¹The Glauber Model is used to calculate “geometrical” parameters of a collision like an impact parameter, number of participating nucleons or number of binary collisions.

space-time evolution of the fireball, the thermal equilibrium is reached. When the system is in the thermal equilibrium the local phase-space densities of particles follow the Fermi-Dirac or Bose-Einstein statistical distributions. At the end of the plasma expansion, the freeze-out occurs. The freeze-out model incorporated in the THERMINATOR model assumes, that chemical and thermal freeze-out occur at the same time.

2.2.1 Cooper-Frye formalism

The result of the hydrodynamic calculations is the freeze-out hypersurface Σ^μ . A three-dimensional element of the surface is defined as [19]

$$d\Sigma_\mu = \epsilon_{\mu\alpha\beta\gamma} \frac{\partial x^\alpha}{\partial \alpha} \frac{\partial x^\beta}{\partial \beta} \frac{\partial x^\gamma}{\partial \gamma} d\alpha d\beta d\gamma, \quad (2.5)$$

where $\epsilon_{\mu\alpha\beta\gamma}$ is the Levi-Civita tensor and the variables $\alpha, \beta, \gamma \in \{1, 2, 3\}$ are used to parametrize the three-dimensional freeze-out hypersurface in the Minkowski four-dimensional space. The Levi-Civita tensor is equal to 1 when the indices form an even permutation (eg. ϵ_{0123}), to -1 when the permutation is odd (e.g. ϵ_{2134}) and has a value of 0 if any index is repeated. Therefore [19],

$$d\Sigma_0 = \begin{vmatrix} \frac{\partial x}{\partial \alpha} & \frac{\partial x}{\partial \beta} & \frac{\partial x}{\partial \gamma} \\ \frac{\partial y}{\partial \alpha} & \frac{\partial y}{\partial \beta} & \frac{\partial y}{\partial \gamma} \\ \frac{\partial z}{\partial \alpha} & \frac{\partial z}{\partial \beta} & \frac{\partial z}{\partial \gamma} \end{vmatrix} d\alpha d\beta d\gamma \quad (2.6)$$

and the remaining components are obtained by cyclic permutations of t, x, y and z .

One can obtain the number of hadrons produced on the hypersurface Σ^μ from the Cooper-Frye formalism. The following integral yields the total number of created particles [19]:

$$N = (2s + 1) \int \frac{d^3 p}{(2\pi)^3 E_p} \int d\Sigma_\mu p^\mu f(p_\mu u^\mu), \quad (2.7)$$

where $f(p_\mu u^\mu)$ is the phase-space distribution of particles (for stable ones and resonances). One can simply derive from Eq. 2.7, the dependence of the momentum density [24]:

$$E \frac{d^3 N}{dp^3} = \int d\Sigma_\mu f(p_\mu u^\mu) p^\mu. \quad (2.8)$$

The momentum distribution f contains non-equilibrium corrections:

$$f = f_0 + \delta f_{shear} + \delta f_{bulk}, \quad (2.9)$$

where

$$f_0(p_\mu u^\mu) = \left\{ \exp \left[\frac{p_\mu u^\mu - (B\mu_B + I_3\mu_{I_3} + S\mu_S + C\mu_C)}{T} \right] \pm 1 \right\}^{-1} \quad (2.10)$$

421 In case of fermions, in the Eq. 2.10 there is a plus sign and for bosons, minus
 422 sign respectively. The thermodynamic quantities appearing in the $f_0(\cdot)$ are T -
 423 temperature, μ_B - baryon chemical potential, μ_{I_3} - isospin chemical potential, μ_S
 424 - strange chemical potential, μ_C - charmed chemical potential and the s is a spin of
 425 a particle. The hydrodynamic calculations yield the flow velocity at freeze-out as
 426 well as the stress and bulk viscosity tensors required to calculate non-equilibrium
 427 corrections to the momentum distribution used in Eq. 2.7. The term coming from
 428 shear viscosity has a form [22]

$$\delta f_{shear} = f_0(1 \pm f_0) \frac{1}{2T^2(e + p)} p^\mu p^\nu \pi_{\mu\nu} \quad (2.11)$$

429 and bulk viscosity

$$\delta f_{bulk} = C f_0(1 \pm f_0) \left(\frac{(u^\mu p_\mu)^2}{3u^\mu p_\mu} - c_s^2 u^\mu p_\mu \right) \Pi \quad (2.12)$$

430 where c_s is sound velocity and

$$\frac{1}{C} = \frac{1}{3} \frac{1}{(2\pi)^3} \sum_{hadrons} \int d^3p \frac{m^2}{E} f_0(1 \pm f_0) \left(\frac{p^2}{3E} - c_s^2 E \right). \quad (2.13)$$

431 The equations presented above are directly used in the THERMINATOR to gen-
 432 erate the primordial hadrons (created during freeze-out) with the Monte-Carlo
 433 method. Resonances produced in this way, propagate and decay, in cascades if
 434 necessary. For every generated particle, its origin point either on a hypersurface
 435 or is associated with the point of the decay of the parent particle. This informa-
 436 tion is kept in the simulation due to its importance for the femtoscopic analysis.

⁴³⁷ **Chapter 3**

⁴³⁸ **Particle interferometry**

⁴³⁹ Two-particle interferometry (also called *femtoscopy*) gives a possibility to
⁴⁴⁰ investigate space-time characteristics of the particle-emitting source created
⁴⁴¹ in heavy ion collisions. Through the study of particle correlations, their
⁴⁴² momentum distributions can be used to obtain information about the spatial
⁴⁴³ extent of the created system. Using this method, one can measure sizes of the
⁴⁴⁴ order of 10^{-15} m and time of the order of 10^{-23} s.

⁴⁴⁵ **3.1 HBT interferometry**

⁴⁴⁶ In the 1956 Robert Hanbury Brown and Richard Q. Twiss proposed a
⁴⁴⁷ method which through analysis of interference between photons allowed to
⁴⁴⁸ investigate angular dimensions of stars. The most important result from the
⁴⁴⁹ Hanbury-Brown-Twiss experiments is that two indistinguishable particles can
⁴⁵⁰ produce an interference effect. There is almost no difference between normal
⁴⁵¹ interferometry and HBT method, except that the latter one does not take into
⁴⁵² account information about phase shift of registered particles. At the beginning
⁴⁵³ this method was used in astronomy for photon interference, but this effect can
⁴⁵⁴ be used also to measure extent of any emitting source. This method was adapted
⁴⁵⁵ to heavy ion collisions to investigate dimensions of a system created in those
⁴⁵⁶ collisions by studying correlations of identical particles [25]. The main difference
⁴⁵⁷ between HBT method in astronomy and femtoscopy is that the first one is based
⁴⁵⁸ on space-time HBT correlations and the latter one uses momentum correlations.
⁴⁵⁹ The momentum correlations yield the space-time picture of the source, whereas
⁴⁶⁰ the space-time HBT correlations provide the characteristic relative momenta of
⁴⁶¹ emitted photons, which gives the angular size of the star without the knowledge
⁴⁶² of its radius and lifetime [10].

463 3.2 Theoretical approach

464 Intensity interferometry in heavy ion physics uses similar mathematical form-
 465 alism as the astronomy HBT measurement. Through the measurement of corre-
 466 lation between particles as a function of their relative momentum one can deduce
 467 the average separation between emitting sources.

468 3.2.1 Conventions used

469 In heavy ion collisions to describe particular directions, components of mo-
 470 mentum and location of particles, one uses naming convention called the Bertsch-
 Pratt coordinate system. This system is presented in the Fig. 3.1. The three dir-

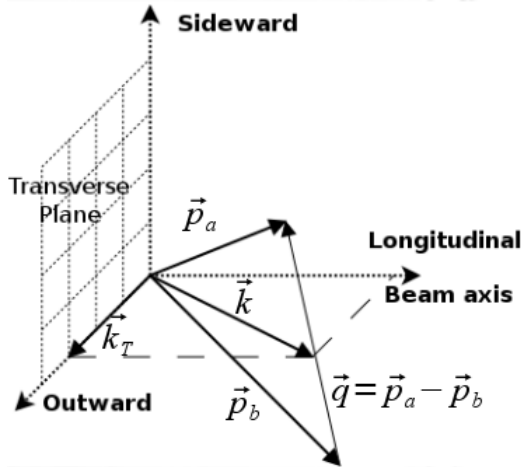


Figure 3.1: Bertsch-Pratt direction naming convention used in heavy ion collision.

471 ections are called *longitudinal*, *outward* and *sideward*. The longitudinal direction
 472 is parallel to the beam axis. The plane perpendicular to the beam axis is called
 473 a *transverse plane*. A projection of a particle pair momentum $\mathbf{k} = (\mathbf{p}_a + \mathbf{p}_b)/2$
 474 on a transverse plane (a *transverse momentum* \mathbf{k}_T) determines *outward* direction:
 475 $(\mathbf{k})_{out} = \mathbf{k}_T$. A direction perpendicular to the longitudinal and outward is called
 476 *sideward*.

477 A particle pair is usually described using two coordinate systems. The first
 478 one, *Longitudinally Co-Moving System* (**LCMS**) is moving along the particle pair
 479 with the longitudinal direction, in other words, the pair longitudinal momentum
 480 vanishes: $(\mathbf{p}_a)_{long} = -(\mathbf{p}_b)_{long}$. The second system is called *Pair Rest Frame* (**PRF**).
 481 In the PRF the centre of mass rests: $\mathbf{p}_a = -\mathbf{p}_b$. Variables which are expressed in
 482 the PRF are marked with a star (e.g. \mathbf{k}^*).

483 The transition of space-time coordinates from LCMS to PRF is simply
 a boost along the outward direction, with the transverse velocity of the

pair $\beta_T = (\mathbf{v}/c)_{out}$ [25]:

$$r_{out}^* = \gamma_t(r_{out} - \beta_T \Delta t) \quad (3.1)$$

$$r_{side}^* = r_{side} \quad (3.2)$$

$$r_{long}^* = r_{long} \quad (3.3)$$

$$\Delta t^* = \gamma_T(\Delta t - \beta_T r_{out}) , \quad (3.4)$$

where $\gamma_T = (1 - \beta_T^2)^{-1/2}$ is the Lorentz factor. However, in calculations performed in this work the equal time approximation is used, which assumes that particles in a pair were produced at the same time in PRF - the Δt^* is neglected.

The most important variables used to describe particle pair are their total momentum $\mathbf{P} = \mathbf{p}_a + \mathbf{p}_b$ and relative momentum $\mathbf{q} = \mathbf{p}_a - \mathbf{p}_b$. In the PRF one has $\mathbf{q} = 2\mathbf{k}^*$, where \mathbf{k}^* is a momentum of the first particle in PRF.

3.2.2 Two particle wave function

Let us consider two identical particles with momenta \mathbf{p}_1 and \mathbf{p}_2 emitted from space points \mathbf{x}_1 and \mathbf{x}_2 . Those emitted particles can be treated as two incoherent waves. If the particles are identical, they are also indistinguishable, therefore one

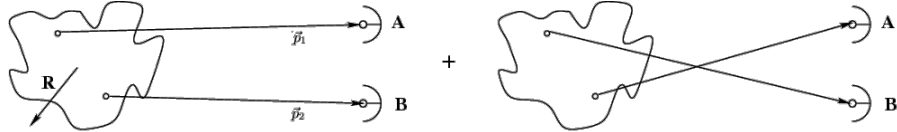


Figure 3.2: The pair wave function is a superposition of all possible states. In case of particle interferometry it includes two cases: particles with momenta p_1, p_2 registered by detectors A, B and p_1, p_2 registered by B, A respectively.

has also take into account the scenario, where the particle with momentum \mathbf{p}_1 is emitted from \mathbf{x}_2 and particle \mathbf{p}_2 from \mathbf{x}_1 (Fig. 3.2). In such case, the wave function describing behaviour of a pair has to contain both components [8]:

$$\Psi_{ab}(\mathbf{q}) = \frac{1}{\sqrt{2}} [\exp(-i\mathbf{p}_1\mathbf{x}_1 - i\mathbf{p}_2\mathbf{x}_2) \pm \exp(-i\mathbf{p}_2\mathbf{x}_1 - i\mathbf{p}_1\mathbf{x}_2)] . \quad (3.5)$$

A two particle wave function of identical bosons is symmetric ("+" sign in Eq. 3.5) and in case of identical fermions - antisymmetric ("−" sign). This anti-symmetrization or symmetrization implies the correlation effect coming from the Fermi-Dirac or Bose-Einstein statistics accordingly.

To provide full description of a system consisting of two charged hadrons, one has to include in the wave function besides quantum statistics also Coulomb and strong Final State Interactions. Considering identical particles systems, the quantum statistics is a main source of a correlation. Hence, in case of space-time analysis of particle emitting source, effects coming from the Coulomb and Strong interactions can be neglected.

507 **3.2.3 Source emission function**

508 To describe particle emitting source, one uses a single emission function [25]:

509

$$S_A(\mathbf{x}_1, \mathbf{p}_1) = \int S(\mathbf{x}_1, \mathbf{p}_1, \mathbf{x}_2, \mathbf{p}_2, \dots, \mathbf{x}_N, \mathbf{p}_N) d\mathbf{x}_2 d\mathbf{p}_2 \dots d\mathbf{x}_N d\mathbf{p}_N \quad (3.6)$$

510 and a two-particle one:

$$S_{AB}(\mathbf{x}_1, \mathbf{p}_1, \mathbf{x}_2, \mathbf{p}_2) = \int S(\mathbf{x}_1, \mathbf{p}_1, \mathbf{x}_2, \mathbf{p}_2, \dots, \mathbf{x}_N, \mathbf{p}_N) d\mathbf{x}_3 d\mathbf{p}_3 \dots d\mathbf{x}_N d\mathbf{p}_N . \quad (3.7)$$

511 Emission function $S(\cdot)$ can be interpreted as a probability to emit a particle, or
 512 a pair of particles from a given space-time point with a given momentum. In
 513 principle, the source emission function should encode all physics aspects of the
 514 particle emission process i.e. the symmetrization for bosons and fermions, as
 515 well as the two-body and many body Final State Interactions. Instead of this,
 516 one assume that each particle's emission process is independent - the interac-
 517 tion between final-state particles after their creation is independent from their
 518 emission process. The assumption of this independence allows to construct two-
 519 particle emission function from single particle emission functions via a convolu-
 520 tion [25]:

$$S(\mathbf{k}^*, \mathbf{r}^*) = \int S_A(\mathbf{p}_1, \mathbf{x}_1) S_B(\mathbf{p}_2, \mathbf{x}_2) \delta \left[\mathbf{k}^* - \frac{\mathbf{p}_1 + \mathbf{p}_2}{2} \right] \delta [\mathbf{r}^* - (\mathbf{x}_1 + \mathbf{x}_2)] \times d^4 \mathbf{x}_1 d^4 \mathbf{x}_2 d^4 \mathbf{x}_1 d^3 \mathbf{p}_1 d^3 \mathbf{p}_2 \quad (3.8)$$

521 In case of identical particles, ($S_A = S_B$) several simplifications can be made.
 522 A convolution of the two same Gaussian distributions is also a Gaussian distri-
 523 bution with σ multiplied by $\sqrt{2}$. Femtoscopy can give information only about
 524 two-particle emission function, but when considering Gaussian distribution as
 525 a source function in Eq. 3.8, one can obtain a σ of a single emission function
 526 from a two-particle emission function. The Eq. 3.8 is not reversible - an inform-
 527 ation about $S_A(\cdot)$ cannot be derived from $S_{AB}(\cdot)$. An exception from this rule
 528 is a Gaussian source function, hence it is often used in femtoscopic calculations.
 529 Considering pairs of identical particles, an emission function is assumed to be
 530 described by the following equation in the Pair Rest Frame [25]:

$$S_{1D}^{PRF}(\mathbf{r}^*) = \exp \left(-\frac{r_{out}^{*2} + r_{side}^{*2} + r_{long}^{*2}}{4R_{inv}^2} \right) . \quad (3.9)$$

To change from the three-dimensional variables to the one-dimensional variable
 one requires introduction of the proper Jacobian r^{*2} .

$$S_{1D}^{PRF}(r^*) = r^{*2} \exp \left(-\frac{r^{*2}}{4R_{inv}^2} \right) . \quad (3.10)$$

531 The “4” in the denominator before the “standard deviation” R_{inv} in the Gaussian
 532 distribution comes from the convolution of the two Gaussian distributions,
 533 which multiplies the R_{inv} by a factor of $\sqrt{2}$.

A more complex form of emission function was used by all RHIC and SPS experiments in identical pion femtoscopy:

$$S_{3D}^{LCMS}(\mathbf{r}) = \exp \left(-\frac{r_{out}^2}{4R_{out}^2} - \frac{r_{side}^2}{4R_{side}^2} - \frac{r_{long}^2}{4R_{long}^2} \right). \quad (3.11)$$

534 The main difference of this source function is that it has three different and inde-
 535 pendent widths R_{out} , R_{side} , R_{long} and they are defined in the LCMS, not in PRF.
 536 Unlike in PRF, in LCMS an equal-time approximation is not used. For identical
 537 particles this is not a problem - only Coulomb interaction inside a wave function
 538 depends on Δt .

539 Relationship between one-dimensional and three-dimensional source sizes

540 Up to now, most of femtoscopic measurements were limited only to averaged
 541 source size R_{av}^L (the letter “L” in superscript stands for LCMS):

$$S_{1D}^{LCMS}(\mathbf{r}) = \exp \left(-\frac{r_{out}^2 + r_{side}^2 + r_{long}^2}{2R_{av}^L} \right). \quad (3.12)$$

542 The relationship between between $S_{1D}^{LCMS}(\cdot)$ and $S_{3D}^{LCMS}(\cdot)$ is given by:

$$S_{3D}^{LCMS}(r) = \int \exp \left(-\frac{r_{out}^2}{2R_{out}^L} - \frac{r_{side}^2}{2R_{side}^L} - \frac{r_{long}^2}{2R_{long}^L} \right) \times \delta \left(r - \sqrt{r_{out}^2 + r_{side}^2 + r_{long}^2} \right) dr_{out} dr_{side} dr_{long}. \quad (3.13)$$

543 The one-dimensional source size corresponding to the three-dimensional one can
 544 be approximated by the following form:

$$S_{1D}^{LCMS}(r) = r^2 \exp \left(-\frac{r^2}{2R_{av}^L} \right). \quad (3.14)$$

545 The equation above assumes that $R_{out}^L = R_{side}^L = R_{long}^L$ hence $R_{av}^L = R_{out}^L$. If this
 546 condition is not satisfied, one can not give explicit mathematical relation between
 547 one-dimensional and three-dimensional source sizes. However, for realistic val-
 548 ues of R (i.e. for similar values of R_{out} , R_{side} , R_{long}), the S_{3D}^{LCMS} from Eq. 3.13 is
 549 not very different from Gaussian distribution and can be well approximated by
 550 Eq. 3.13.

551 A deformation of an averaged source function in case of big differences in
 552 R_{out} , R_{side} , R_{long} is presented in the Fig. 3.3. A three-dimensional Gaussian dis-
 553 tribution with varying widths was averaged into one-dimensional function using

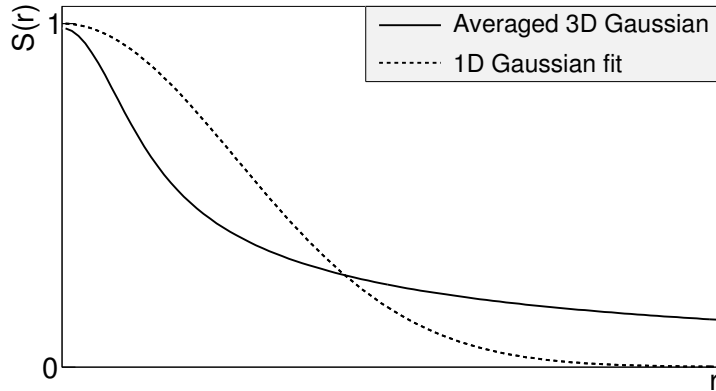


Figure 3.3: An averaged three-dimensional Gaussian source function with different widths was averaged into one-dimensional function. To illustrate deformations, one-dimensional Gaussian distribution was fitted.

the Eq. 3.13. Afterwards, an one-dimensional Gaussian distribution was fitted.
 One can notice a heavy tail of an averaged distribution in long r region, which
 makes an approximation using one-dimensional distribution in this case quite
 inaccurate.

Using Eq. 3.13 and Eq. 3.14 one can obtain a relation between one-dimensional width and the three-dimensional ones. Through numerical calculations one can find the following approximate relation [25]:

$$R_{av}^L = \sqrt{\left(R_{out}^L\right)^2 + \left(R_{side}^L\right)^2 + \left(R_{long}^L\right)^2} / 3 . \quad (3.15)$$

This equation does not depend on the pair velocity, hence it is valid in the LCMS and PRF.

3.2.4 Theoretical correlation function

The fundamental object in a particle interferometry is a correlation function.
 The correlation function is defined as:

$$C(\mathbf{p}_a, \mathbf{p}_b) = \frac{P_2(\mathbf{p}_a, \mathbf{p}_b)}{P_1(\mathbf{p}_a)P_1(\mathbf{p}_b)} , \quad (3.16)$$

where P_2 is a conditional probability to observe a particle with momentum \mathbf{p}_b if particle with momentum \mathbf{p}_a was also observed. A P_1 is a probability to observe a particle with a given momentum. The relationship between source emission function, pair wave function and the correlation function is described by the following equation:

$$C(\mathbf{p}_1, \mathbf{p}_2) = \int S_{AB}(\mathbf{p}_1, \mathbf{x}_1, \mathbf{p}_2, \mathbf{x}_2) |\Psi_{AB}|^2 d^4\mathbf{x}_1 d^4\mathbf{x}_2 \quad (3.17)$$

Substituting the one-dimensional emission function (Eq. 3.10) into the integral above yields the following form of correlation function in PRF:

$$C(q) = 1 + \lambda \exp(-R_{inv}^2 q^2) \quad (3.18)$$

where q is a momentum difference between two particles. When using the three-dimensional emission function (Eq. 3.11) one gets the following correlation function defined in the LCMS:

$$C(\mathbf{q}) = 1 + \lambda \exp(-R_{out}^2 q_{out}^2 - R_{side}^2 q_{side}^2 - R_{long}^2 q_{long}^2) \quad (3.19)$$

568 where q_{out} , q_{side} , q_{long} are \mathbf{q} components in the outward, sideward and longitudinal direction. The λ parameter in the equations above determines correlation
 569 strength. The lambda parameter has values in the range $\lambda \in [-0.5, 1]$ and it depends on a pair type. In case of pairs of identical bosons (like $\pi\pi$ or KK) the
 570 lambda parameter $\lambda \rightarrow 1$. For identical fermions (e.g. $p-p$) $\lambda \rightarrow -0.5$. Values of
 571 λ observed experimentally are lower than 1 (for bosons) and greater than -0.5
 572 (for fermions). There are few explanations to this effect: detector efficiencies,
 573 inclusion of misidentified particles in a used sample or inclusion of non-correlated
 574 pairs (when one or both particles come from e.g. long-lived resonance). The
 575 analysis carried out in this work uses data from a model, therefore the detector
 576 efficiency and particle purity is not taken into account [25].
 577

579 3.2.5 Spherical harmonics decomposition of a correlation function

580 Results coming from an analysis using three-dimensional correlation function
 581 in Cartesian coordinates are quite difficult to visualize. To do that, one usually
 582 performs a projection into a one dimension in outward, sideward and longitudinal
 583 directions. One may loose important information about a correlation
 584 function in this procedure, because it gives only a limited view of the full three-
 585 dimensional structure. Recently, a more advanced way of presenting correlation
 586 function - a spherical harmonics decomposition, was proposed. The three-
 587 dimensional correlation function is decomposed into an infinite set of components
 588 in a form of one-dimensional histograms $C_l^m(q)$. In this form, a correlation
 589 function is defined as a sum of a series [26]:

$$C(\mathbf{q}) = \sum_{l,m} C_l^m(q) Y_l^m(\theta, \phi), \quad (3.20)$$

590 where $Y_l^m(\theta, \phi)$ is a spherical harmonic function. Spherical harmonics are an
 591 orthogonal set of solutions to the Laplace's equation in spherical coordinates
 592 Hence, in this approach, a correlation function is defined as a function of q , θ
 593 and ϕ . To obtain C_l^m coefficients in the series, one has to calculate the following
 594 integral:

$$C_l^m(q) = \int_{\Omega} C(q, \theta, \phi) Y_l^m(\theta, \phi) d\Omega, \quad (3.21)$$

595 where Ω is a full solid angle.

Spherical harmonics representation has several important advantages. The main advantage of this decomposition is that it requires less statistics than traditional analysis performed in Cartesian coordinates. Another one is that it encodes full three-dimensional information in a set of one-dimensional plots. In principle it does not have to be an advantage, because full description of a correlation function requires infinite number of l, m components. But it so happens that the intrinsic symmetries of a pair distribution in a femtoscopic analysis result in most of the components to vanish. For the identical particles correlation functions, all coefficients with odd values of l and m disappear. It has also been shown, that the most significant portion of femtoscopic data is stored in the components with the lowest l values. It is expected that, the main femtoscopic information is contained in the following components [25]:

$$C_0^0 \rightarrow R_{LCMS}, \quad (3.22)$$

$$\Re C_2^0 \rightarrow \frac{R_T}{R_{long}}, \quad (3.23)$$

$$\Re C_2^2 \rightarrow \frac{R_{out}}{R_{side}}, \quad (3.24)$$

596 where $R_{LCMS} = \sqrt{(R_{out}^2 + R_{side}^2 + R_{long}^2)/3}$ and $R_T = \sqrt{(R_{out}^2 + R_{side}^2)/2}$.
 597 The C_0^0 is sensitive to the overall size of a correlation function. The $\Re C_2^0$ carries
 598 the information about the ratio of the transverse to the longitudinal radii, due
 599 to its $\cos^2(\theta)$ weighting in Y_2^0 . The component $\Re C_2^2$ with its $\cos^2(\phi)$ weighting
 600 encodes the ratio between outward and sideward radii. Thus, the spherical har-
 601 monics method allows to obtain and analyze full three-dimensional femtoscopic
 602 information from a correlation function [25].

603 3.3 Experimental approach

604 The correlation function is defined as a probability to observe two particles
 605 together divided by the product of probabilities to observe each of them sepa-
 606 rately (Eq. 3.16). Experimentally this is achieved by dividing two distributions
 607 of relative momentum of pairs of particles coming from the same event and the
 608 equivalent distribution of pairs where each particle is taken from different colli-
 609 sions. In this way, one obtains not only femtoscopic information but also all other
 610 event-wide correlations. This method is useful for experimentalists to estimate
 611 the magnitude of non-femtoscopic effects. There exists also a different approach,
 612 where two particles in pairs in the second distribution are also taken from the
 613 same event. The second method gives only information about physical effects
 614 accessible via femtoscopy. The aim of this work is a study of effects coming from
 615 two particle interferometry, hence the latter method was used.

616 In order to calculate experimental correlation function, one uses the follow-
 617 ing approach. One has to construct two histograms: the *numerator* N and the

618 denominator D with the particle pairs momenta, where particles are coming from
 619 the same event. Those histograms can be one-dimensional (as a function of $|\mathbf{q}|$),
 620 three dimensional (a function of three components of \mathbf{q} in LCMS) or a set of one-
 621 dimensional histogram representing components of the spherical harmonic de-
 622 composition of the distribution. The second histogram, D is filled for each pair
 623 with the weight 1.0 at a corresponding relative momentum $\mathbf{q} = 2\mathbf{k}^*$. The first one,
 624 N is filled with the same procedure, but the weight is calculated as $|\Psi_{ab}(\mathbf{r}^*, \mathbf{k}^*)|^2$.
 625 A division N/D gives the correlation function C . This procedure can be simply
 626 written as [25]:

$$C(\mathbf{k}^*) = \frac{N}{D} = \frac{\sum_{n_i \in D} \delta(\mathbf{k}^* i - \mathbf{k}^*) |\Psi_{ab}(\mathbf{r}^* i, \mathbf{k}^* i)|^2}{\sum_{n_i \in D} \delta(\mathbf{k}^* i - \mathbf{k}^*)} . \quad (3.25)$$

The D histogram represents the set of all particle pairs used in calculations.
 The n_i is a pair with the its relative momentum $\mathbf{k}^* i$ and relative separation $\mathbf{r}^* i$.
 The wave function used in Eq. 3.25 has one of the following forms:

$$|\Psi_{\pi\pi}(\mathbf{r}^*, \mathbf{k}^*)|^2 = |\Psi_{KK}(\mathbf{r}^*, \mathbf{k}^*)|^2 = 1 + \cos(2\mathbf{k}^* \mathbf{r}^*) , \quad (3.26)$$

$$|\Psi_{pp}(\mathbf{r}^*, \mathbf{k}^*)|^2 = 1 - \frac{1}{2} \cos(2\mathbf{k}^* \mathbf{r}^*) . \quad (3.27)$$

627 The first one is used in case of bosons, and the latter one is for identical fermi-
 628 ons. Mathematically, the procedure of calculating the Eq. 3.25 is equivalent to a
 629 calculation of an integral in Eq. 3.17 through a Monte-Carlo method.

630 3.4 Scaling of femtoscopic radii

631 In the hydrodynamic models describing expansion of a quark-gluon plasma,
 632 particles are emitted from the source elements. Each of the source elements is
 633 moving with the velocity u_μ given by hydrodynamic equations. Because solu-
 634 tions of those equations are smooth, nearby source elements have similar velo-
 635 cities. Each emitted particle from a certain source element is boosted with the
 636 flow velocity u_μ according to the point of origin. Hence particles emitted close
 637 to each other (pairs with large transverse momentum $|\mathbf{k}_T|$) will gain the similar
 638 velocity boost, they can combine into pairs with small relative momenta ($|\mathbf{q}|$) and
 639 therefore become correlated. If the two particles are emitted far away from each
 640 other (a pair with small $|\mathbf{k}_T|$), the flow field u_μ in their point of emission might
 641 be very different and it will be impossible for them to have sufficiently small rel-
 642 ative momenta in order to be in region of interference effect. This effect is visible
 643 in a width of a correlation function in the Fig. 3.4. The correlation function gets
 644 broader for greater values of $|\mathbf{k}_T|$ and the femtoscopic radius R becomes smal-
 645 ler [8, 27].

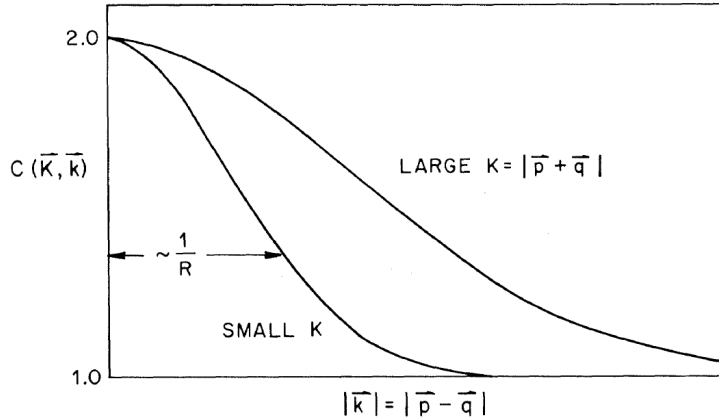


Figure 3.4: Correlation function width dependence on total pair momentum. Pion pairs with a large total momentum are more correlated [27].

646 3.4.1 Scaling in LCMS

Hydrodynamic calculations performed in LCMS show that femtoscopic radii in outward, sideward, and longitudinal direction show dependence on transverse mass $m_T = \sqrt{k_T^2 + m^2}$, where m is a mass of a particle [28]. Moreover, experimental results show that this scaling is observed for R_{LCMS} radii also. This dependence can be expressed as follows:

$$R_i = \alpha m_T^{-\beta} \quad (3.28)$$

647 where i subscript indicates that this equation applies to R_{out} , R_{side} and R_{long}
 648 radii. The β exponent is approximately equal 0.5. In case of strong transversal
 649 expansion of the emitting source, the decrease of longitudinal interferometry ra-
 650 dius can be more quick than $m_T^{-0.5}$, hence one can expect for longitudinal radii
 651 greater values of $\beta > 0.5$ [28].

652 3.4.2 Scaling in PRF

653 In the collisions at the LHC energies, pions are most abundant particles and
 654 their multiplicities are large enough to enable three-dimensional analysis. How-
 655 ever, for heavier particles, such as kaons and protons statistical limitations arise.
 656 Hence it is often possible to only measure one-dimensional radius R_{inv} for those
 657 particles. The R_{inv} is then calculated in the PRF. The transition from LCMS to
 658 PRF is a Lorentz boost in the direction of pair transverse momentum with velo-
 659 city $\beta_T = p_T/m_T$. Hence only R_{out} radius changes:

$$R_{out}^* = \gamma_T R_{out}. \quad (3.29)$$

660 The one-dimensional R_{inv} radius is direction-averaged source size in PRF. One
 661 can notice, that such power-law scaling of R_{inv} described by Eq. 3.28 is not

662 observed. To recover such scaling in PRF one has to take into consideration two
 663 effects when transforming variables from LCMS to PRF: overall radius growths
 664 and source distribution becomes non-Gaussian, while developing long-range
 665 tails (see Fig. 3.3 for an example). The interplay of these two effects can be
 666 accounted with an approximate formula:

$$R_{inv} = \sqrt{(R_{out}^2 \sqrt{\gamma_T} + R_{side}^2 + R_{long}^2)/3} . \quad (3.30)$$

Assuming that all radii are equal $R_{out} = R_{side} = R_{long}$ this formula can be simplified:

$$R_{LCMS} \approx R_{inv} \times [(\sqrt{\gamma_T} + 2)/3]^{-1/2} . \quad (3.31)$$

667 This approximate formula allows to restore power-law behaviour of the scaled
 668 radii not only when the radii are equal, but also when their differences are small
 669 (for explanation see the last part of the section 3.2.3).

670 This method of recovering scaling in PRF can be used as a tool for the search
 671 of hydrodynamic collectivity between pions, kaons and protons in heavy ion col-
 672 lisions with the measurement of one-dimensional radius in PRF.

673 **Chapter 4**

674 **Results**

675 For the purposes of the femtoscopic analysis in this thesis, the THERMINATOR
676 model was used to generate large number of events for eight different sets of
677 initial conditions corresponding the following centrality ranges: 0-5%, 0-10%, 10-
678 20%, 20-30%, 30-40%, 40-50%, 50-60% and 60-70% for the Pb-Pb collisions at the
679 centre of mass energy $\sqrt{s_{NN}} = 2.76 \text{ TeV}$.

680 **4.1 Identical particles correlations**

681 The correlation functions (three-dimensional and one-dimensional) were cal-
682 culated separately for the following different pairs of identical particles: π - π , K -
683 K and p - p for nine k_T bins (in GeV/c): 0.1-0.2, 0.2-0.3, 0.3-0.4, 0.4-0.5, 0.6-0.7,
684 0.7-0.8, 0.8-1.0 and 1.0-1.2. In case of kaons, k_T ranges start from 0.3 and for pi-
685 ons from 0.4 and for both of them the maximum value is 1.0. The k_T ranges for
686 the heavier particles were limited to maintain sufficient multiplicity to perform
687 reliable calculations.

688 **4.1.1 Spherical harmonics components**

689 The three-dimensional correlation function as a function of relative
690 momentum q_{LCMS} was calculated in a form of components of spherical
691 harmonics series accordingly to the Eq. 3.21. In the femtoscopic analysis of
692 identical particles, the most important information is stored in the $\Re C_0^0$, $\Re C_2^0$
693 and $\Re C_2^2$, hence only those components were analyzed. Correlation functions
694 obtained in this procedure were calculated for the different centrality bins for the
695 pairs of pions, kaons and protons. They are presented in the Fig. 4.1, 4.2 and 4.3.

696 Coefficients for pairs of identical bosons (pions and kaons) are shown in the
697 Fig. 4.1 and 4.2. The wave function symmetrization (Bose-Einstein statistics)
698 causes the increase of a correlation in the low relative momenta regime ($q_{LCMS} <$
699 0.06 GeV/c or even $q_{LCMS} < 0.12 \text{ GeV/c}$ for more peripheral collisions). It is
700 clearly visible in the $\Re C_0^0$ component. The $\Re C_0^0$ resembles one-dimensional cor-

relation function and in fact it encodes information about overall source radius. The second coefficient $\Re C_2^0$ differs from zero (is negative), which yields the information about the ratio R_T/R_{long} . The $\Re C_2^2$ stores the R_{out}/R_{side} ratio and one can notice that is non-vanishing (is also negative).

The correlation function for a pair of identical fermions is presented in the Fig. 4.3. An influence of wave function anti-symmetrization (Fermi-Dirac statistics) has its effect in the decrease of a correlation down to 0.5 at low relative momentum ($q_{LCMS} < 0.1 \text{ GeV/c}$ or $q_{LCMS} < 0.15 \text{ GeV/c}$ for more peripheral collisions), which can be observed in $\Re C_0^0$. The $\Re C_2^0$ and $\Re C_2^2$ coefficients differ from zero and are becoming positive.

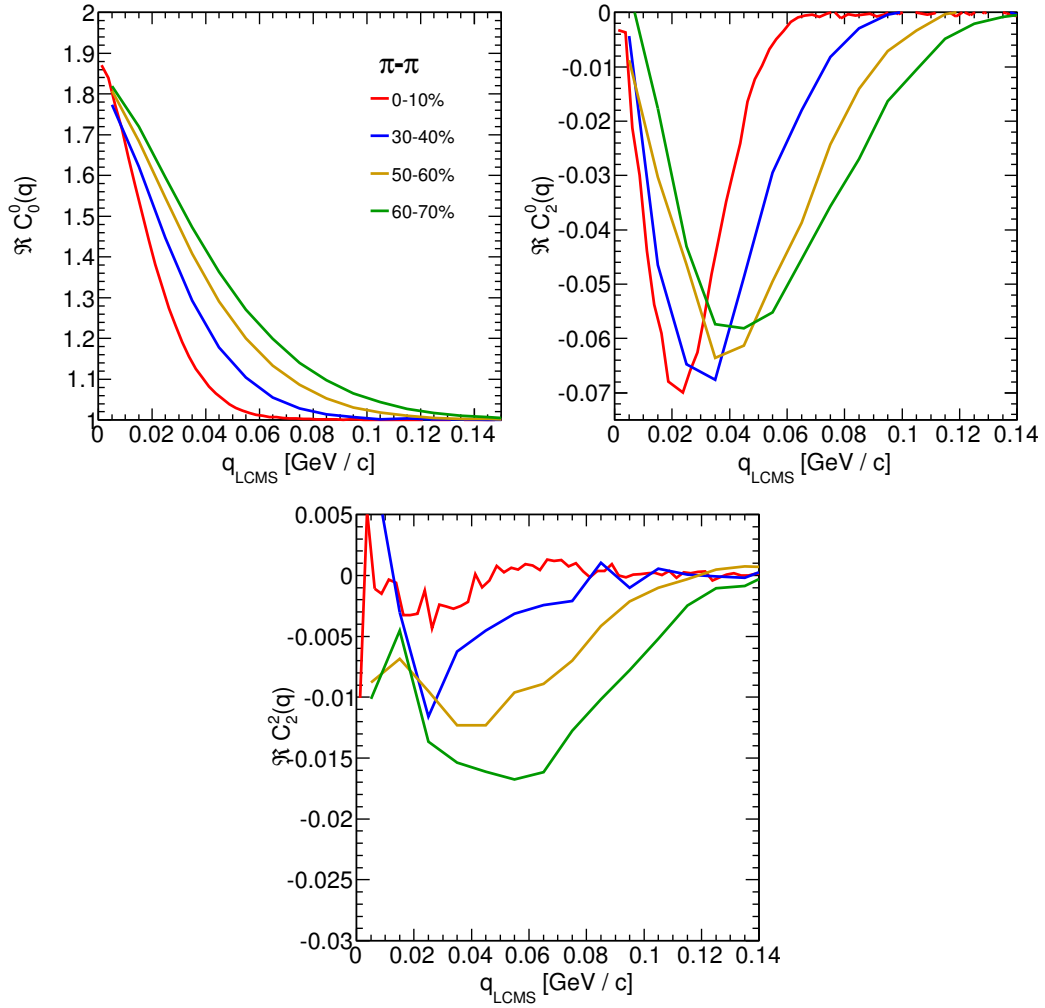


Figure 4.1: Spherical harmonics coefficients of the two-pion correlation function. From the top left: $\Re C_0^0$, $\Re C_2^0$ and $\Re C_2^2$. Only few centrality bins are presented for increased readability.

The common effect of the spherical harmonics form of a correlation function is the “mirroring” of the shape of the $\Re C_0^0$ coefficient - when correlation function increases at low q_{LCMS} , the $\Re C_2^0$ and $\Re C_2^2$ are becoming negative and vice versa. This is quite different behaviour than in the case of correlations of non-identical particles, where the $\Re C_2^0$ still behaves in the same manner, but $\Re C_2^2$ has the opposite sign to the $\Re C_2^0$ [25].

In all cases, the correlation function gets wider with the peripherality of a collision i.e. the correlation function for most central collisions (0-10%) is much narrower than for the most peripheral ones (60-70%). This phenomena in clearly

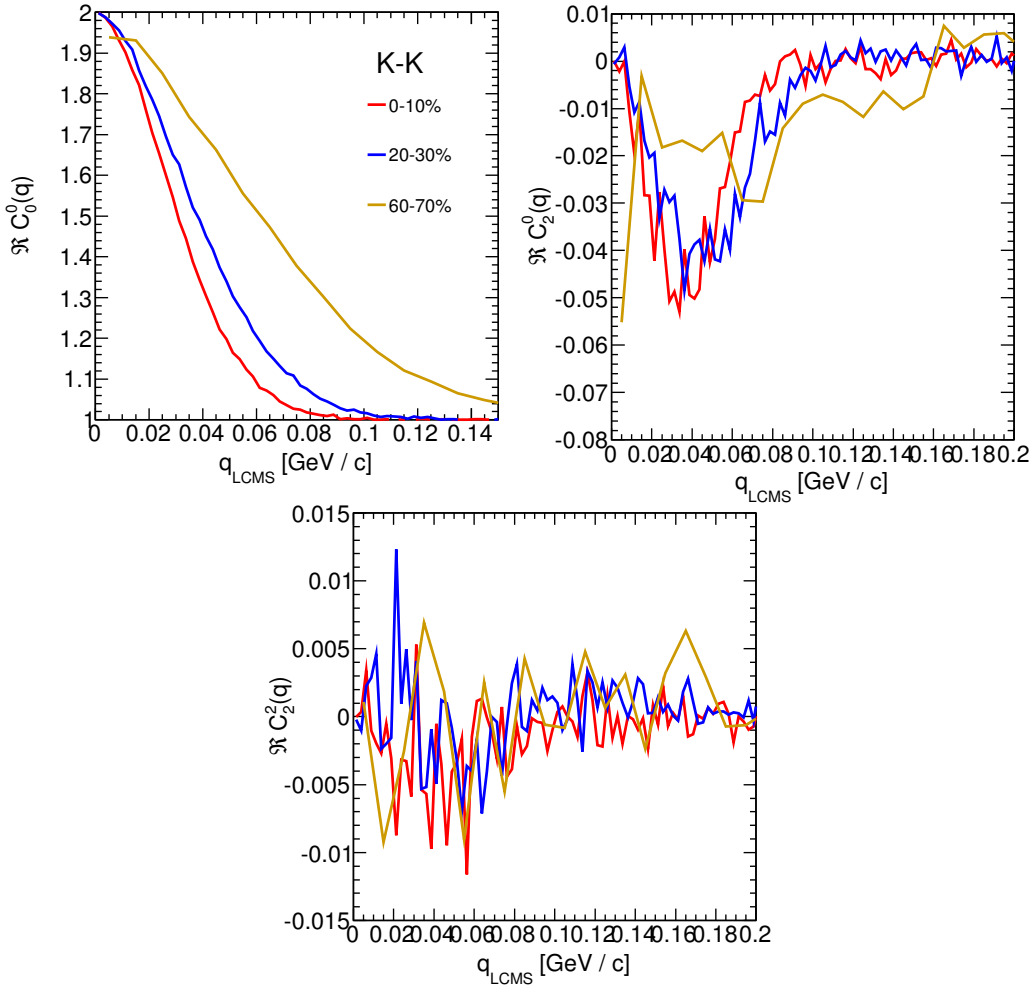


Figure 4.2: Spherical harmonics coefficients of the two-kaon correlation function. From the top left: $\Re C_0^0$, $\Re C_2^0$ and $\Re C_2^2$. Only few centrality bins are presented for increased readability. The $\Re C_2^2$ is noisy, but one can still notice that it differs from zero and is becoming negative.

visible the $\Re C_0^0$ coefficients. Other components are also affected by this effect, this is especially noticeable in the case of kaons and pions. For the protons, the results are noisy, hence this effect is not clearly distinguishable.

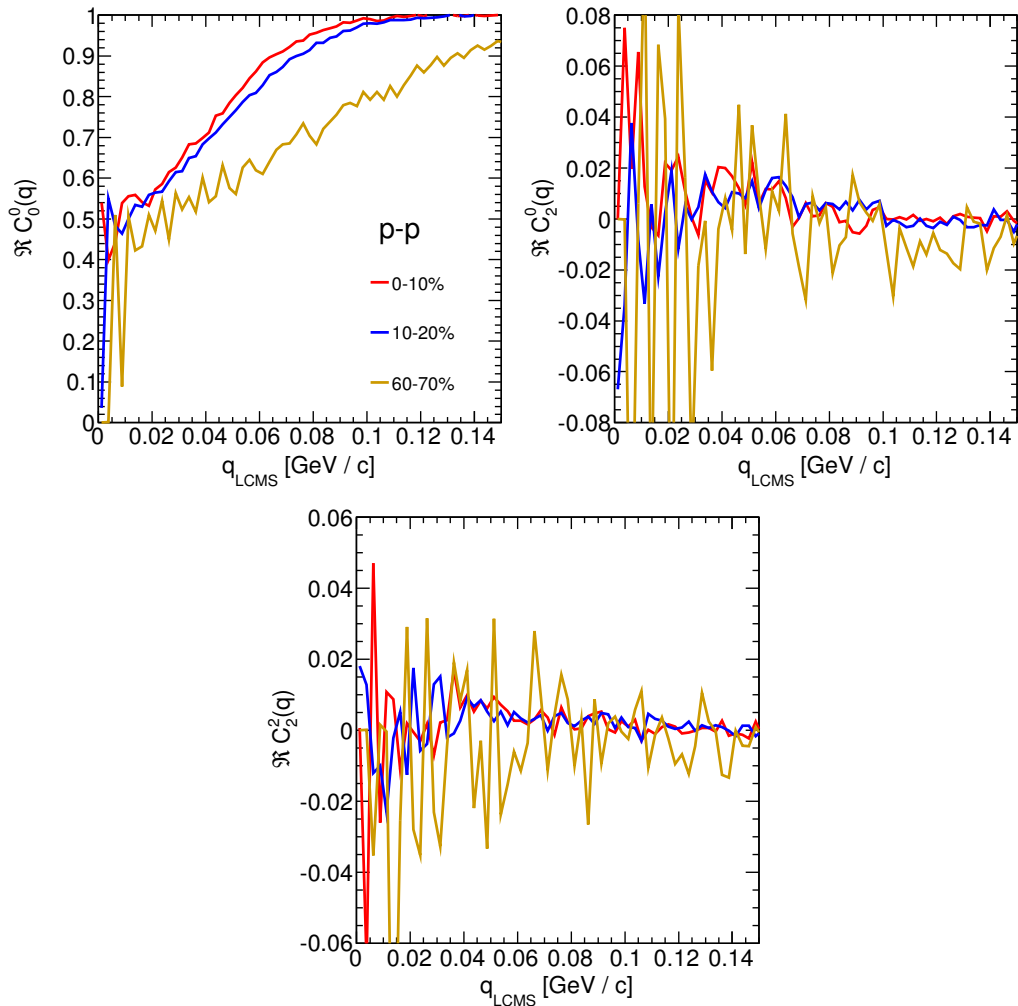


Figure 4.3: Spherical harmonics coefficients of the two-proton correlation function. From the top left: $\Re C_0^0$, $\Re C_2^0$ and $\Re C_2^2$. Only few centrality bins are presented for increased readability. The $\Re C_2^0$ and $\Re C_2^2$ are noisy, but one can still notice, that they differ from zero and are becoming positive.

723 **4.1.2 Centrality dependence of a correlation function**

724 The centrality dependence of a correlation function is especially visible in
 725 one-dimensional correlation functions. This effect is presented in the Fig. 4.4 -
 726 the correlation functions for pions, kaons and protons are plotted for the same
 727 k_T range but different centrality bins. One can notice that the width of a func-
 728 tion is smaller in the case of most central collisions. Hence, the femtoscopic radii
 729 (proportional to the inverse of width) are increasing with the centrality. An ex-
 730 planation for this growth is that in the most central collisions, a size of a created
 system is larger than for the peripheral ones.

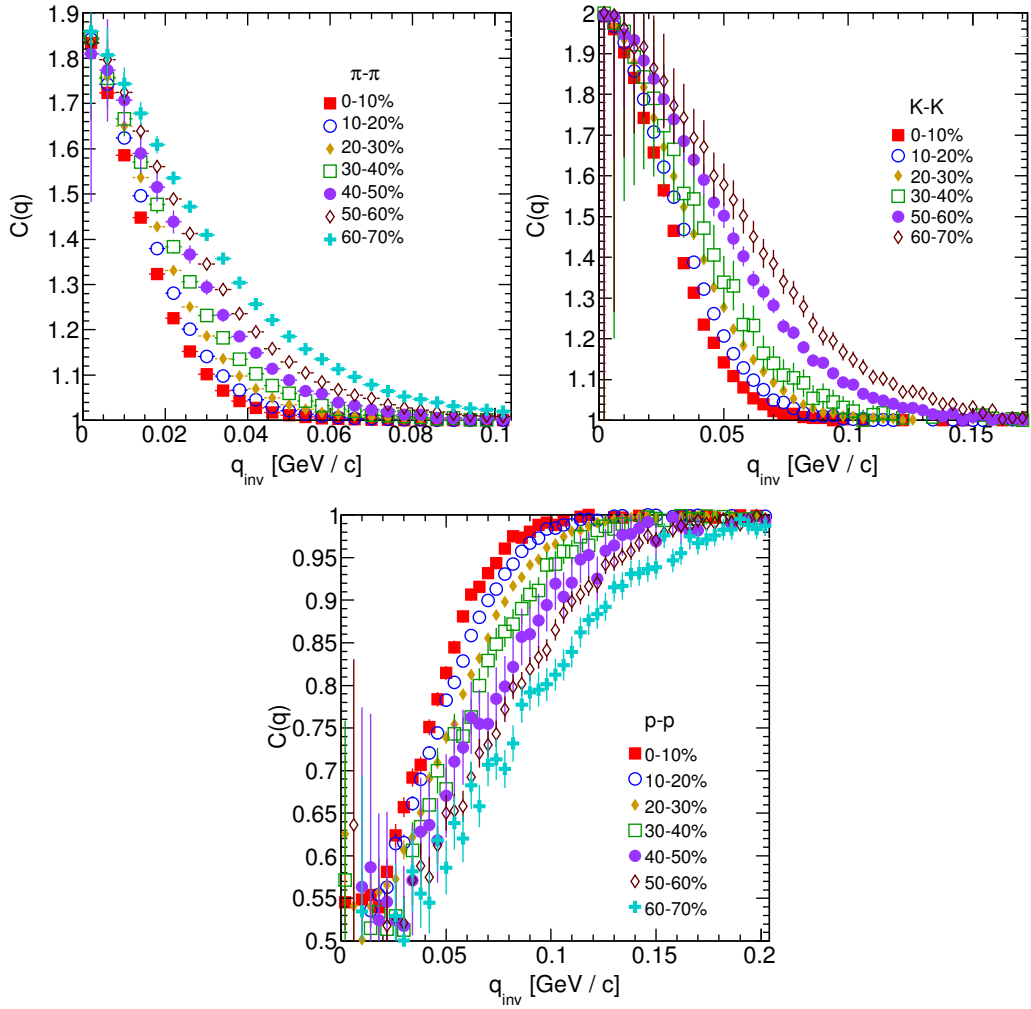


Figure 4.4: One-dimensional correlation function for pions (top left), kaons (top right) and protons (bottom) for different centralities.

4.1.3 k_T dependence of a correlation function

In the Fig. 4.5 there are presented one-dimensional correlation functions for pions, kaons and protons for the same centrality bin, but different k_T ranges. One can observe in all cases of the particle types, appearance of the same trend: with the increase of the total transverse momentum of a pair, the width of a correlation function increases and the femtoscopic radius decreases. The plots in the Fig. 4.5 were zoomed in to show the influence of k_T .

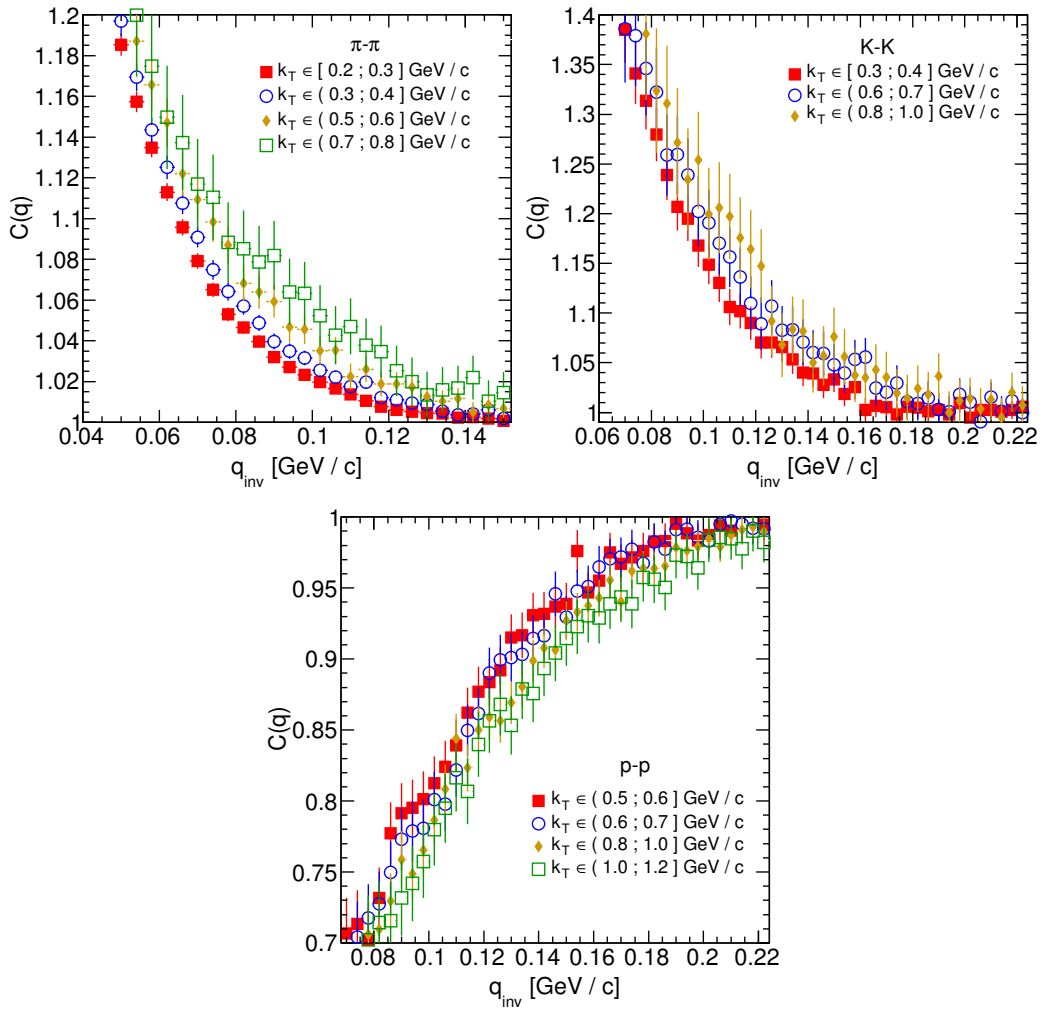


Figure 4.5: One-dimensional correlation functions for pions, kaons and protons, for the same centrality bin and different k_T ranges. The plot was zoomed in to the region which illustrates the k_T dependence in the best way. Only few of the calculated ranges are presented for better readability.

4.2 Results of the fitting procedure

In order to perform a quantitative analysis of a wide range of correlation functions, the theoretical formulas were fitted to the calculated experimental-like data. In this procedure, the femtoscopic radii for the three-dimensional as well as one-dimensional correlation functions were extracted. The main goal of this analysis is a verification of a common transverse mass scaling for different particles types. Obtained radii are plotted as a function of a transverse mass $m_T = \sqrt{k_T^2 + m^2}$. To test the scaling, the following power-law was fitted to the particular radii afterwards:

$$R_x = \alpha m_T^{-\beta}, \quad (4.1)$$

where the α and β are free parameters.

4.2.1 The three-dimensional femtoscopic radii scaling

In the Fig. 4.6 there are presented femtoscopic radii in the outward, sideward and longitudinal directions for the analysis of two-pion correlation functions in

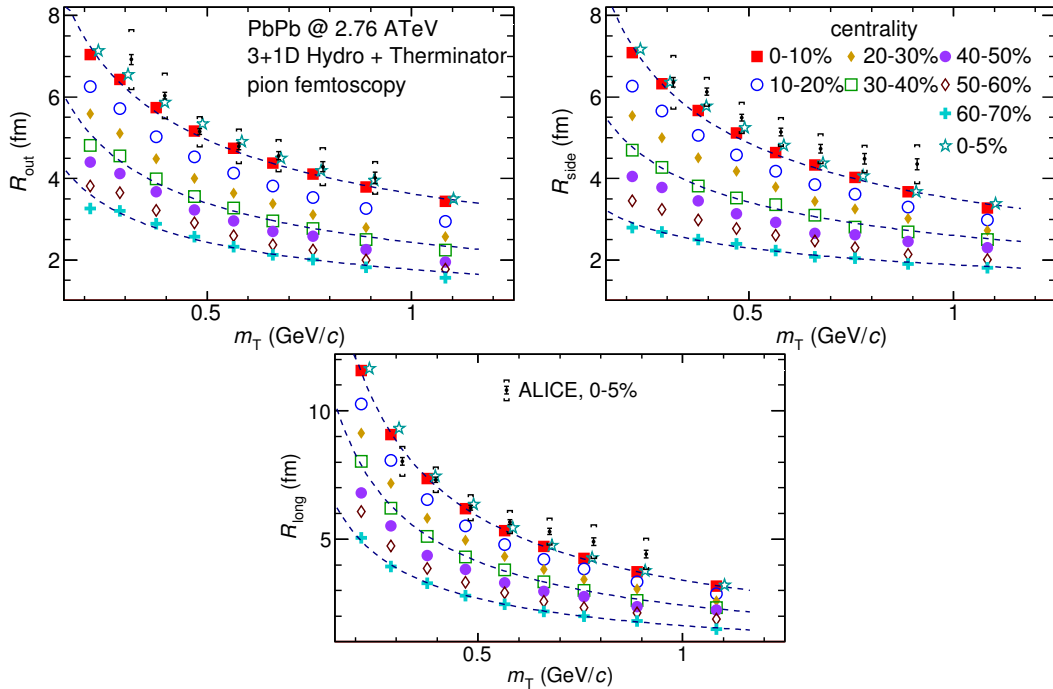


Figure 4.6: Femtoscopic radii in LCMS coming from two-pion correlation functions for all centrality bins as a function of m_T . The dashed lines are power-law fits. The most central collisions (0-5%) are compared to the results from ALICE [29]. The two datasets are shifted to the right for visibility [30].

the LCMS. The dashed lines are fits of the power law to the data. One can notice, that the power law describes well data points with a 5% accuracy. The β fit parameter for the outward direction is in the order of 0.45. For the sideward direction, this parameter has the similar value, but it is lower for the most peripheral collisions. In case of the longitudinal direction, the β has greater value, up to 0.75. In the Fig. 4.6 there are also compared results for the top 5% central collisions (star-shaped markers) with experimental data from ALICE [29]. The experimental results are consistent with the ones coming from the model predictions.

The Fig. 4.7 presents femtoscopic radii coming from the kaon calculations. The R_{out} , R_{side} and R_{long} fall also with the power-law within the 5% accuracy. The β parameter was larger in case of kaons: 0.59 in outward direction, 0.54 in the sideward and 0.86 for longitudinal.

The results for two-proton analysis are shown in the Fig. 4.8. The Eq. 4.1 was fitted to the data and tells that the protons also follow the m_T scaling within 5% range. The β parameter values were even bigger for the outward (0.58), sideward (0.61) and longitudinal (1.09) directions than for the other particle types.

The Fig. 4.9 presents results for the pions, kaons and protons together as a function of m_T . Considering differences in the β value for the fits for differ-

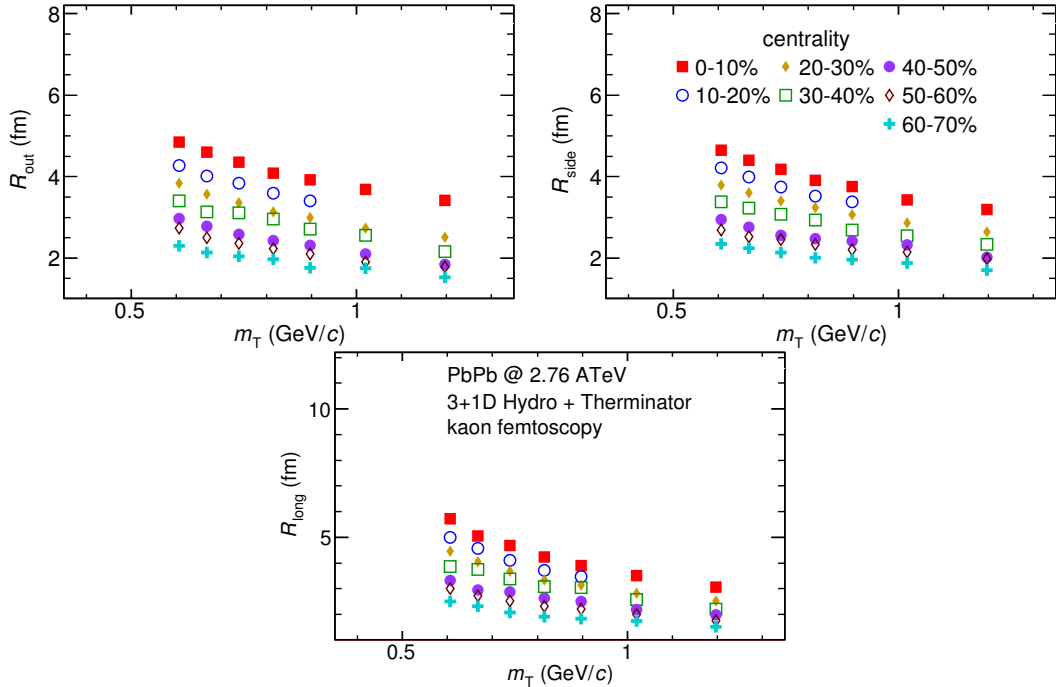


Figure 4.7: Femtoscopic radii extracted from two-kaon correlation functions for different centrality bins as a function of m_T . [30].

ent particles, one can suspect that there is no common scaling between different kinds of particles. However, when all of the results shown on the same plot, they are aligning on the common curve and the scaling is well preserved. The scaling accuracy is 3%, 5% and 4% for the 0-10%, 20-30% and 60-70% for the outward direction. For the sideward radii the scaling is better, with average deviations 2%, 2% and 3% respectively. In case of longitudinal direction the accuracy is 6%, 5% and 3% for the three centralities. The β parameter for the outward direction is close to the 0.42 in all cases. For the sideward direction it varies from 0.28 to 0.47 and is bigger for more central collisions. Regarding longitudinal radii, the exponent is bigger than the other two: $\beta \in [0.62; 0.72]$. Considering all results, the plotted radii are following the common power-law scaling within the 5% accuracy for all directions, centralities and particle types.

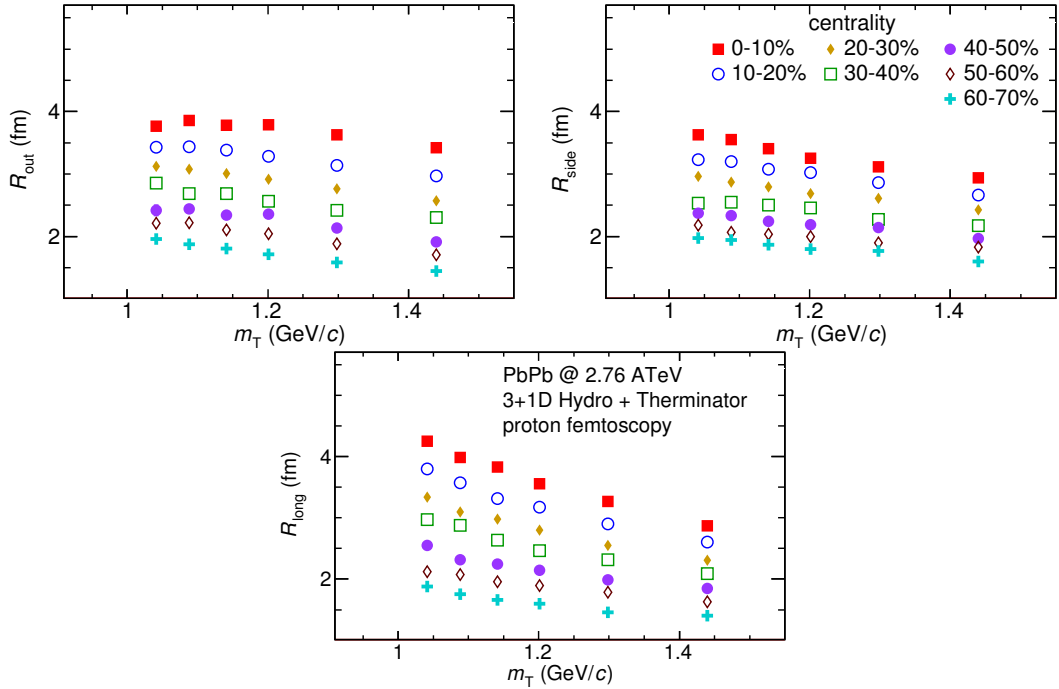


Figure 4.8: Femtoscopic radii extracted from two-proton correlation functions for different centrality bins as a function of m_T . [30].

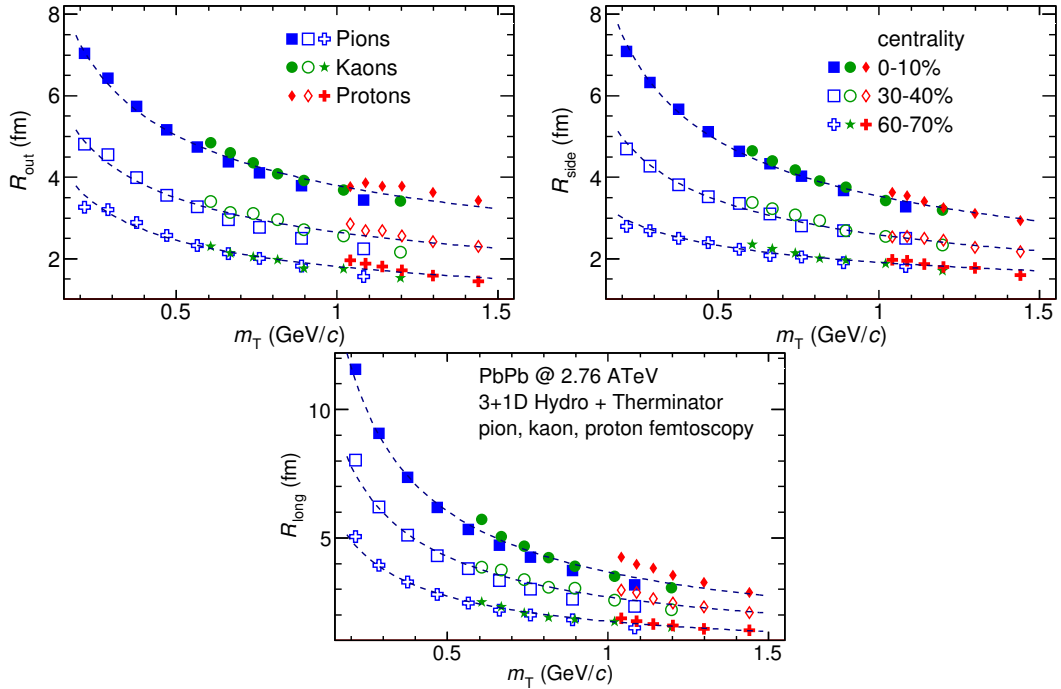


Figure 4.9: The results from the calculations for the pions, kaons and protons in for the three centralities presented on the common plot. One can notice that radii for particular centralities and different particle types follow the common power-law scaling. [30].

4.2.2 Scaling of one-dimensional radii

To the one-dimensional correlation function, the corresponding function in the PRF given by the Eq. 3.18 was fitted. The results from those fits are presented in the upper left plot in the Fig. 4.10. One immediately notices, that there is no common scaling of R_{inv} for different kind of particles. In the Fig. 4.9 the radii in the outward direction for the pions, kaons and protons for the same m_T are similar. However, when one performs a transition from the LCMS to the PRF, the R_{out} radius grows:

$$R_{out}^* = \gamma_T R_{out}, \quad (4.2)$$

where $\gamma_T = m_T/m$. For the lighter particles, the γ_T is much larger, hence the bigger growth of the R_{out} and the overall radius. This is visible in the Fig. 4.10 (top left), where the radii in the PRF for the lighter particles are bigger than for the heavier ones in case of the same m_T range.

In the Fig. 4.9 there is visible scaling in the outward, sideward and longitudinal direction. Hence one can expect an appearance of such scaling in a direction-averaged radius calculated in the LCMS. This radius is presented in the Fig. 4.10 (bottom) and indeed the R_{LCMS} exhibits power-law scaling with the m_T .

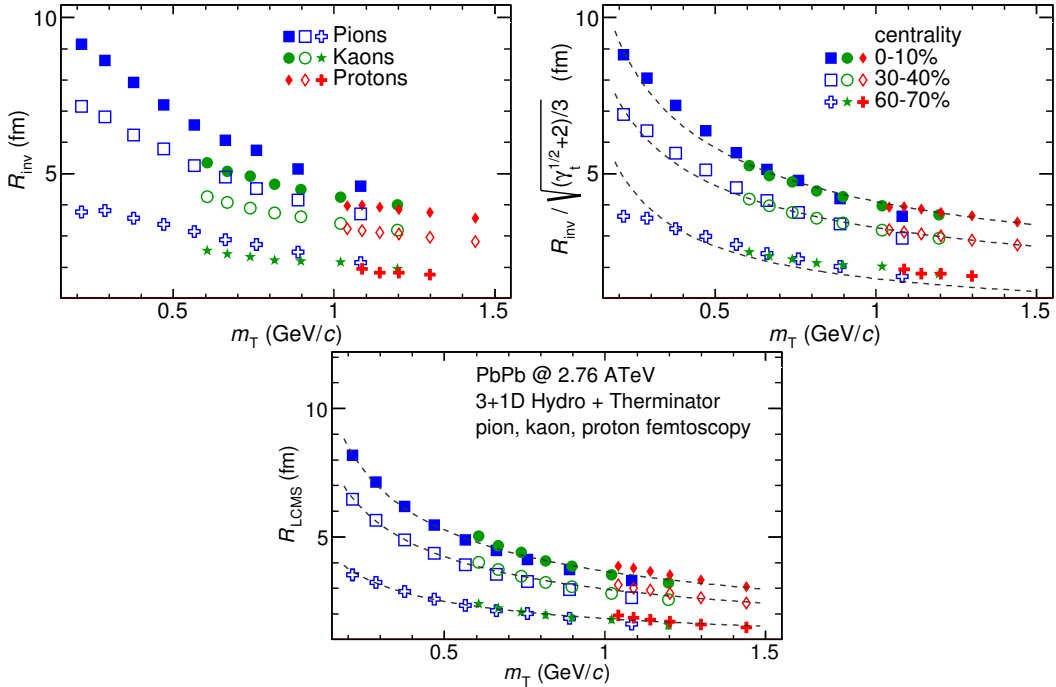


Figure 4.10: Top left: one-dimensional radius for pions, kaons and protons calculated in the PRF. Top right: the R_{inv} scaled by the proposed factor. Bottom: averaged one-dimensional radius in the LCMS for pions, kaons and protons. Only three centrality bins are shown for the better readability [30].

800 One can try to account the effect of an increase of the radii in the outward
 801 direction by using the appropriate scaling factor. In the Fig. 4.10 (top right) there
 802 are femtoscopic radii in the LCMS divided by the proposed scaling factor:

$$f = \sqrt{(\sqrt{\gamma_T} + 2)/3} . \quad (4.3)$$

803 The radii for pions, kaons and protons in the PRF after the division by f are
 804 following the power-law with the accuracy of 10%.

805 4.3 Discussion of the results

806 The femtoscopic radii obtained from the three-dimensional correlation func-
 807 tion fitting exhibit the m_T dependence described by the power law (Eq. 4.1). This
 808 scaling is preserved quite well with accuracy <10%. Observation of such scaling
 809 in a femtoscopic radii is a strong signal of appearance of a collective behaviour of
 810 a particle-emitting source created in the collision. The data used in the analysis
 811 was coming from the hydrodynamic model, hence one can indeed expect the
 812 appearance of this scaling. However, the results for pion femtoscopy from the
 813 ALICE at LHC are consistent with the data from analysis performed in this thesis
 814 (Fig. 4.6). This is a confirmation of an applicability of hydrodynamic models in a
 815 description of an evolution of a quark-gluon plasma.

816 The β parameter calculated in the fitting of the power-law to the femtoscopic
 817 radii is in the order of 0.5 in case of the radii in the transverse plane. This value is
 818 consistent with the hydrodynamic predictions. In case of longitudinal radii, the
 819 exponent is bigger (greater than 0.7), which is an indication of a strong transversal
 820 expansion in the system [28].

821 A scaling described above is visible in the LCMS, however due to limited stat-
 822 istics, analysis in this reference frame is not always possible. In such case one per-
 823 forms calculations in the PRF. The m_T scaling in the PRF is not observed - this has
 824 the trivial kinematic origin. A transition from the PRF to LCMS causes growth
 825 of the radius in the outward direction and the common power-law scaling for
 826 different particles breaks due to differences in the $\gamma_T(m_T)$ for different particle
 827 types. However one can try to deal with the radius growth and restore the scal-
 828 ing by multiplying the radii R_{inv} by an approximate factor $\sqrt{(\sqrt{\gamma_T} + 2)/3}$. The
 829 scaled R_{inv} are following the power-law and could be used as a verification of
 830 hydrodynamic behaviour in the investigated particle source.

831 The hadronic evolution and freeze-out in the THERMINATOR is followed by
 832 the resonance propagation and decay phase. A good accuracy of a scaling with
 833 the power-law indicated that the inclusion of the resonances does not break the
 834 m_T scaling. However, recent calculations including also hadron rescattering
 835 phase indicate that the scaling between pions and kaons is broken at LHC [31].

⁸³⁶ **Chapter 5**

⁸³⁷ **Summary**

838 **Bibliography**

- 839 [1] Standard Model of Elementary Paticles - Wikipedia, the free encyclopedia
840 http://en.wikipedia.org/wiki/standard_model.
- 841 [2] R. Aaij et al. (LHCb Collaboration). Observation of the resonant character of
842 the $z(4430)^-$ state. *Phys. Rev. Lett.*, 112:222002, Jun 2014.
- 843 [3] Donald H. Perkins. *Introduction to High Energy Physics*. Cambridge University Press,
844 fourth edition, 2000. Cambridge Books Online.
- 845 [4] G. Odyniec. *Phase Diagram of Quantum Chromo-Dynamics* - course at Faculty
846 of Physics, Warsaw University of Technology, Jun 2012.
- 847 [5] J. Beringer et al. (Particle Data Group). The Review of Particle Physics. *Phys.*
848 *Rev.*, D86:010001, 2012.
- 849 [6] Z. Fodor and S.D. Katz. The Phase diagram of quantum chromodynamics.
850 2009.
- 851 [7] F. Karsch. Lattice results on QCD thermodynamics. *Nuclear Physics A*, 698(1-
852 4):199 – 208, 2002.
- 853 [8] Adam Kisiel. *Studies of non-identical meson-meson correlations at low relative ve-*
854 *locities in relativistic heavy-ion collisions registered in the STAR experiment*. PhD
855 thesis, Warsaw University of Technology, Aug 2004.
- 856 [9] J. Bartke. *Relativistic Heavy Ion Physics*. World Scientific Pub., 2009.
- 857 [10] W. Florkowski. *Phenomenology of Ultra-Relativistic Heavy-Ion Collisions*.
858 World Scientific, 2010.
- 859 [11] Science Grid This Week, October 25, 2006 - Prob-
860 ing the Perfect Liquid with the STAR Grid
861 http://www.interactions.org/sgtw/2006/1025/star_grid_more.html.
- 862 [12] K. Grebieszkow. Fizyka zderzeń ciężkich jonów,
863 <http://www.if.pw.edu.pl/~kperl/hip/hip.html>.
- 864 [13] Ulrich W. Heinz. From SPS to RHIC: Maurice and the CERN heavy-ion
865 programme. *Phys.Scripta*, 78:028005, 2008.

- 866 [14] J. Adams et al. Identified particle distributions in pp and Au+Au collisions
867 at $s(\text{NN})^{**}(1/2) = 200 \text{ GeV}$. *Phys.Rev.Lett.*, 92:112301, 2004.
- 868 [15] G. David, R. Rapp, and Z. Xu. Electromagnetic Probes at RHIC-II. *Phys.Rept.*,
869 462:176–217, 2008.
- 870 [16] A. Marin et al. Dilepton measurements with CERES. *PoS*, CPOD07:034,
871 2007.
- 872 [17] J. Adams et al. Experimental and theoretical challenges in the search for the
873 quark gluon plasma: The STAR Collaboration’s critical assessment of the
874 evidence from RHIC collisions. *Nucl.Phys.*, A757:102–183, 2005.
- 875 [18] Adam Kisiel, Tomasz Taluc, Wojciech Broniowski, and Wojciech
876 Florkowski. THERMINATOR: THERMal heavy-IoN generATOR. *Comput.Phys.Commun.*, 174:669–687, 2006.
- 878 [19] Mikolaj Chojnacki, Adam Kisiel, Wojciech Florkowski, and Wojciech Bro-
879 niowski. THERMINATOR 2: THERMal heavy IoN generATOR 2. *Comput.Phys.Commun.*, 183:746–773, 2012.
- 881 [20] I. et al (BRAHMS Collaboration) Bearden. Charged meson rapidity distri-
882 butions in central Au + Au collisions at $\sqrt{s_{\text{NN}}} = 200 \text{ GeV}$. *Phys. Rev. Lett.*,
883 94:162301, Apr 2005.
- 884 [21] W. Israel and J.M. Stewart. Transient relativistic thermodynamics and kin-
885 etic theory. *Annals of Physics*, 118(2):341 – 372, 1979.
- 886 [22] Piotr Bożek. Flow and interferometry in (3 + 1)-dimensional viscous hydro-
887 dynamics. *Phys. Rev. C*, 85:034901, Mar 2012.
- 888 [23] K. Kovtun, P. D. T. Son, and A. O. Starinets. Viscosity in strongly interacting
889 quantum field theories from black hole physics. *Phys. Rev. Lett.*, 94:111601,
890 Mar 2005.
- 891 [24] Fred Cooper and Graham Frye. Single-particle distribution in the hydro-
892 dynamic and statistical thermodynamic models of multiparticle production.
893 *Phys. Rev. D*, 10:186–189, Jul 1974.
- 894 [25] Adam Kisiel. Nonidentical-particle femtoscopy at $\sqrt{s_{\text{NN}}} = 200 \text{ GeV}$ in hy-
895 drodynamics with statistical hadronization. *Phys. Rev. C*, 81:064906, Jun
896 2010.
- 897 [26] Adam Kisiel and David A. Brown. Efficient and robust calculation of femto-
898 scopic correlation functions in spherical harmonics directly from the raw
899 pairs measured in heavy-ion collisions. *Phys.Rev.*, C80:064911, 2009.
- 900 [27] S. Pratt. Pion Interferometry for Exploding Sources. *Phys.Rev.Lett.*, 53:1219–
901 1221, 1984.

- 902 [28] S.V. Akkelin and Yu.M. Sinyukov. The HBT-interferometry of expanding
903 inhomogeneous sources. *Z.Phys.*, C72:501–507, 1996.
- 904 [29] K. Aamodt et al. Two-pion Bose-Einstein correlations in central Pb-Pb colli-
905 sions at $\sqrt{s_{NN}} = 2.76$ TeV. *Phys.Lett.*, B696:328–337, 2011.
- 906 [30] A. Kisiel, M. Galazyn, and P. Bozek. Pion, kaon, and proton femtoscopy in
907 Pb-Pb collisions at $\sqrt{s_{NN}}=2.76$ TeV modeled in 3+1D hydrodynamics. 2014.
- 908 [31] V.M. Shapoval, P. Braun-Munzinger, Iu.A. Karpenko, and Yu.M. Sinyukov.
909 Femtoscopy correlations of kaons in $Pb + Pb$ collisions at LHC within hy-
910 drokinetic model. 2014.

List of Figures

912 1.1	The Standard Model of elementary particles [1].	2
913 1.2	A string break and a creation of a pair quark-anti-quark [4].	4
914 1.3	The coupling parameter α_s dependence on four-momentum transfer Q^2 [5].	5
915 1.4	The QCD potential for a pair quark-antiquark as a function of distance for different temperatures. A value of a potential decreases with the temperature [4].	5
916 1.5	A number of degrees of freedom as a function of a temperature [7].	6
917 1.6	Phase diagram coming from the Lattice QCD calculations [8].	7
918 1.7	Left: stages of a heavy ion collision simulated in the UrQMD model. Right: schematic view of a heavy ion collision evolution [8].	8
919 1.8	Overlapping region which is created in heavy ion collisions has an almond shape. Visible x-z plane is a <i>reaction plane</i> . The x-y plane is a <i>transverse plane</i> . The z is a direction of the beam [11].	10
920 1.9	Cross-section of a heavy ion collision in a transverse plane. Ψ_R is an angle between transverse plane and the reaction plane. The b parameter is an <i>impact parameter</i> - a distance between centers of nuclei during a collision. An impact parameter is related with the centrality of a collision and a volume of the quark-gluon plasma [12].	11
921 1.10	<i>Lower:</i> The elliptic flow v_2 follows the hydrodynamical predictions for an ideal fluid perfectly. Note that > 99% of all final hadrons have $p_T < 1.5 \text{ GeV}/c$. <i>Upper left:</i> The v_2 plotted versus transverse kinetic energy $KET = m_T - m_0 = \sqrt{p_T^2 + m_0^2} - m_0$. The v_2 follows different universal curves for mesons and baryons. <i>Upper right:</i> When scaled by the number of valence quarks, the v_2 follows the same universal curve for all hadrons and for all values of scaled transverse kinetic energy [13].	12
922 1.11	Invariant yield of particles versus transverse mass $m_T = \sqrt{p_T^2 + m_0^2}$ for π^\pm , K^\pm , p and \bar{p} at mid-rapidity for p+p collisions (bottom) and Au+Au events from 70-80% (second bottom) to 0-5% (top) centrality [14].	13

943	1.12 Thermal photons spectra for the central Au+Au collisions at $\sqrt{s_{NN}} = 200$ GeV at computed within different hydrodynamical models compared with the pQCD calculations (solid line) and experimental data from PHENIX (black dots) [15].	14
947	1.13 Left: Invariant mass spectrum of e^+e^- pairs in Pb+Au collisions at 158A GeV compared to the sum coming from the hadron decays predictions. Right: The expectations coming from model calculations assuming a dropping of the ρ mass (blue) or a spread of the ρ width in the medium (red) [16].	15
952	1.14 Azimuthal angle difference $\Delta\phi$ distributions for different colliding systems at $\sqrt{s_{NN}} = 200$ GeV. Transverse momentum cut: $p_T > 2$ GeV. For the Au+Au collisions the away-side jet is missing [17]. . .	16
955	3.1 Bertsch-Pratt direction naming convention used in heavy ion collision.	22
957	3.2 The pair wave function is a superposition of all possible states. In case of particle interferometry it includes two cases: particles with momenta p_1, p_2 registered by detectors A, B and p_1, p_2 registered by B, A respectively.	23
961	3.3 An averaged three-dimensional Gaussian source function with different widths was averaged into one-dimensional function. To illustrate deformations, one-dimensional Gaussian distribution was fitted.	26
965	3.4 Correlation function width dependence on total pair momentum. Pion pairs with a large total momentum are more correlated [27]. .	30
967	4.1 Spherical harmonics coefficients of the two-pion correlation function. From the top left: $\Re C_0^0$, $\Re C_2^0$ and $\Re C_2^2$. Only few centrality bins are presented for increased readability.	33
970	4.2 Spherical harmonics coefficients of the two-kaon correlation function. From the top left: $\Re C_0^0$, $\Re C_2^0$ and $\Re C_2^2$. Only few centrality bins are presented for increased readability. The $\Re C_2^2$ is noisy, but one can still notice that it differs from zero and is becoming negative. .	34
974	4.3 Spherical harmonics coefficients of the two-proton correlation function. From the top left: $\Re C_0^0$, $\Re C_2^0$ and $\Re C_2^2$. Only few centrality bins are presented for increased readability. The $\Re C_2^0$ and $\Re C_2^2$ are noisy, but one can still notice, that they differ from zero and are becoming positive.	35
979	4.4 One-dimensional correlation function for pions (top left), kaons (top right) and protons (bottom) for different centralities.	36

981	4.5	One-dimensional correlation functions for pions, kaons and protons, for the same centrality bin and different k_T ranges. The plot was zoomed in to the region which illustrates the k_T dependence in the best way. Only few of the calculated ranges are presented for better readability.	37
982	4.6	Femtoscopic radii in LCMS coming from two-pion correlation functions for all centrality bins as a function of m_T . The dashed lines are power-law fits. The most central collisions (0-5%) are compared to the results from ALICE [29]. The two datasets are shifted to the right for visibility [30].	38
983	4.7	Femtoscopic radii extracted from two-kaon correlation functions for different centrality bins as a function of m_T . [30].	39
984	4.8	Femtoscopic radii extracted from two-proton correlation functions for different centrality bins as a function of m_T . [30].	40
985	4.9	The results from the calculations for the pions, kaons and protons in for the three centralities presented on the common plot. One can notice that radii for particular centralities and different particle types follow the common power-law scaling. [30].	41
986	4.10	Top left: one-dimensional radius for pions, kaons and protons calculated in the PRF. Top right: the R_{inv} scaled by the proposed factor. Bottom: averaged one-dimensional radius in the LCMS for pions, kaons and protons. Only three centrality bins are shown for the better readability [30].	42
987			
988			
989			
990			
991			
992			
993			
994			
995			
996			
997			
998			
999			
1000			
1001			
1002			
1003			